



Shahid Chamran
University of Ahvaz

Journal of Applied and Computational Mechanics



Research Paper

Heat Transfer Enhancement and Boundary Layer Separations for a Hybrid Nanofluid Flow past an Isothermal Cylinder

Nepal Chandra Roy¹, Aysha Akter²

¹ Department of Mathematics, University of Dhaka, Dhaka, Bangladesh, Email: nepal@du.ac.bd

² Department of Mathematics, University of Dhaka, Dhaka, Bangladesh, Email: lizadumath@gmail.com

Received June 21 2021; Revised August 03 2021; Accepted for publication August 03 2021.

Corresponding author: Nepal Chandra Roy (nepal@du.ac.bd)

© 2021 Published by Shahid Chamran University of Ahvaz

Abstract. Unsteady magnetohydrodynamic mixed convection flow of an incompressible hybrid nanofluid (Cu-Al₂O₃/water) past an isothermal cylinder with thermal radiation effect has been studied. Appropriate non-dimensional variables are initiated to reduce the governing equations into a convenient form. By utilizing the procedure of finite difference, reduced equations are then solved for all time. Besides, series solutions are obtained using perturbation technique for short time and asymptotic method for long time which agree with the acquired numerical solution up to a good accuracy. When the mixed convection parameter R_i , radiation conduction parameter R_d , magnetic field parameter M and the volume fractions of nanoparticles ϕ_1 and ϕ_2 are increased, the local skin friction coefficient and the local Nusselt number are found to increase. Results revealed that the hybrid nanofluid (Cu-Al₂O₃/water) enhances the heat transfer about 28.28% in comparison to the Al₂O₃-water nanofluid and about 51.15% than the pure fluid. Contrary to this, the heat transfer of hybrid nanofluid is augmented about 41.76% than the Cu-water nanofluid and 71.41% than the base fluid. The streamlines and isotherms reveal that higher values of R_i , M and R_d delay the boundary layer separation and accordingly shrink the vortices. Moreover, the thermal boundary layer is thickened for the increment of aforesaid quantities. The surface temperature parameter augments the local skin friction coefficient, however, the reverse characteristic is observed for the local Nusselt number.

Keywords: Hybrid nanofluid; Mixed convection; Isothermal cylinder; Boundary layer separation; Thermal radiation.

1. Introduction

Mixed convective heat transfer across a thermally driven cylinder is of great practical interest over decades. When the forced convection is of the order of natural convection, the combined effect of natural and forced convection must be considered. As a result, the heat transfer process of such system is known as a mixed convective heat transfer. Due to simplicity of the geometry and complexity of the physical process a considerable attention has been paid to various aspects of mixed convection flow past a cylinder and therefore it has a great approach found in multitudinous industrial and engineering purpose, notably, electrifying, molding of metals, melted metal flow, manufacturing of petroleum, fusion reactors in the presence of coolant as liquid lithium or liquid sodium [1, 2].

Aldoss et al. [3] analytically studied the radiative hydromagnetic effect on flow and temperature profiles of free-forced convection along a horizontal cylinder. Assuming a variable wall temperature constraint at the cylinder surface, numerical consequences were acquired and substantiated by applying two different numerical procedures. However, Hasan and Ali [4] investigated the thermal performance of mixed convection flow along a heated square cylinder in a range of the Reynolds number. They analyzed bifurcations numerically from the unsteady state to the uniform state and in the reverse pattern also. Recently, Roy et al. [5] inspected the separation points of free-forced convective flow around a circular cylinder. Based on shooting technique, Abel et al. [2] studied the behavior of velocity and temperature profile of upper convective Maxwell's fluid. They introduced several parameters to find the optimized solutions with magnetic field. Azim et al. [6] examined the hydromagnetic free convective flow along a circular cylinder. They discovered the fact that the magnetic field parameter strongly affects the fluid motion and fluid temperature subjected to joule heating as well as thermal manufacture of the system. Moreover, Sharma et al. [7] paid attention to study the thermal performance of mixed convection flow across a square cylinder with the supremacy of alleviating buoyancy force. The onset of flow separation has been also explored for different values of the pertinent parameters. In addition, Das et al. [8] emphasized on the analysis of rotational buoyancy influence on unsteady magnetohydrodynamic flow with thermal radiation whereas Chaabane et al. [9] worked on the thermal performance of radiative fluid flow within a cylindrical media. Furthermore, Wang and Kleinstreuer [10] analyzed the boundary layer separation of mixed convective power-law fluid past a cylinder and a sphere while Mucoglu and Chen [11] summarized the convective free-forced flow over a horizontal cylinder.

It should be mentioned that the above investigations have been carried out for conventional fluids, namely, pure water, propylene glycol, mineral oils, etc. Due to the low thermal performance of these fluids, several authors have paid their attention to



invent the proper ways to augment the heat transportation in the fluid. To amplify the thermal conductivity of base fluid, there is a usage of nano-sized solid metallic components in the performing fluid. This inclusion of solid nanocomponent in the operating fluid is termed as nanofluid. Throughout the recent past, thermal properties of nanofluid have been studied by several researchers due to its great usage in thermal engineering. In 1995, Choi and Eastman [12] first used the concept of nanofluid to develop the heat execution of traditional fluid. Moreover, to minimize the entropy generation in real life problem, Sachica et al. [13] observed the effect of hydromagnetic mixed convection flow in a channel using Al_2O_3 -water nanofluid. A parametric study has been done to find the vorticity dynamics and thermal transport mannerism within the transient entropy generation. Additionally, in the appearance of radiative magnetic field Hosseinzadeh et al. [14] analyzed entropy generation of ethylene glycol where carbon nanotubes are used as nanoparticles. In order to simplify the nonlinear governing equations, they used Runge-Kutta method and performed parametric study to understand their impacts on an entire entropy generation. However, Mkhathshwa et al. [15] numerically studied the mixed convective nanofluid flow around a vertical slender cylinder under magnetic field effect. Most recently, Hayat et al. [16] considered Jeffrey nanofluid to expose the unsteady hydromagnetic flow over a stretching cylinder accompanied by radiation and hydromagnetic impacts. However, Nagendramma et al. [17] inspected the motion of hydromagnetic tangent hyperbolic nanofluid flow across a stretching cylinder whereas Roy et al. [18] reviewed the magnetohydrodynamic mixed convection flow of Al_2O_3 -water nanofluid regarding the diversifications of sinusoidal surface temperature. Sheikholeslami et al. [19, 20] investigated nanofluid impacts on turbulent flow using different geometries. Consequences exposed that elevated flow turbulence causes an increase in fluid velocity as well as heat transportation rate. Moreover, a review has been done by Sheikholeslami et al. [21] numerically to find the better performance of system temperature with multiple nanofluids considering two flat plate collectors.

The chronicle of hybrid nanofluid has come forward in more recent days to provide better thermal conductivity than nanofluid to the functionality of system. An appreciable contemplation of several investigators has enamored with this new-age type of well-versed fluid owing to its massive extent of potential approach in engineering, industries and in other sciences. Applications include power generation, space, automotive industry, biomedical, defense, solar energy, heat exchanger, ventilation, refrigeration, air conditioning, coolant in microelectronics such as nuclear system, generator and transformer cooling where the cooling system is based on different types of fluid medium considering forced flow [22, 23] etc.

For the past few years, researchers are desirous to scrutinize the characteristics of hybrid nanofluid for its promising performance in thermal conduction. In this way, Zainal et al. [24] examined the integrated free-forced hybrid nanofluid flow around a vertically situated flat plate. A benchmark investigation has been done to characterize the magnetic field effects on fluid velocity as well as fluid temperature. However, Alharbi et al. [25] studied both the thermal performance of hydromagnetic hybrid nanofluid and hydromagnetic nanofluid. Furthermore, Khashi'ie et al. [26] carried out the flow and heat transfer characteristics of $\text{Cu-Al}_2\text{O}_3$ /water hybrid nanofluid along a shrinking cylinder. They numerically solved the reduced ordinary differential equations and exposed that boundary layer separation point can be found promptly due to the conjunction of curvature parameter. Meanwhile, considering a hydromagnetic hybrid nanofluid, the stagnation point flow and the rate of heat transfer from a moving cylinder have been experimented by Abbas et al. [27]. A few years ago, Devi and Devi [28] studied the hybrid nanofluid flow over 3-D stretching sheet in the appearance of Lorentz force effect. Very recently, the 3-D radiative hydromagnetic flow of a hybrid nanofluid has been excellently discussed by Shoaib et al. [29]. Considering the viscous material and joule heating, they demonstrated velocity and temperature profiles analytically. In addition, Rashid et al. [30] investigated the different shape of nanoparticles (Ag and TiO_2) on hybrid nanofluid flow to explore their better impact on thermal conductivity. Using the fixed values of Prandtl number, $\text{Pr}=6.2$, they concluded that sphere shaped Ag and TiO_2 nanoparticles provide dramatic performance on heat transfer characteristics. Ghalambaz et al. [31, 32] numerically analyzed the free-forced convection flow past a vertical plate and on natural convection flow respectively. Considering nano-encapsulated materials subjected to phase alteration dispersed in base fluid, heat transfer has been investigated thoroughly in both cases. Later, the same material has also been utilized by Mehryan et al. [33] to substantiate heat transportation increment inside an annulus for free convection flow while Hajjar et al. [34] performed on it for unsteady thermal boundary constraints inside a cavity. Additionally, conjugate free convective and natural convective flow submerged in a porous domain with Ag-MgO hybrid nanofluid has been examined analytically by Ghalambaz et al. [35] and Mehryan et al. [36] consecutively. A set of relevant parameters with Rayleigh number ranging from 10 to 1000 has been regarded to understand fluid flow and temperature profile.

Hence, based on above literature survey, it is clear that the study of unsteady mixed convection flow of a hybrid nanofluid across an isothermal cylinder in classical magnetohydrodynamic problems has not been investigated yet. Even analysis of boundary layer separation from a cylinder requires attention because of controlling the flow and heat transfer past a heated cylinder. Additionally, most of the previous works have been accomplished on the basis of steady state constraint. Therefore, present study investigates the unsteady free-forced flow of $\text{Cu-Al}_2\text{O}_3$ /water hybrid nanofluid past an isothermal circular cylinder. Based on non-dimensional variables, a set of nonlinear partial differential equations are transformed from governing equations. Later, these obtained equations are simplified by utilizing implicit finite difference scheme for all time and then the solutions are verified graphically by comparing with asymptotic solution for long time and perturbation solution for small time. To understand the boundary layer separation characteristics thoroughly of this complex flow, streamlines and isotherms are investigated. Moreover, the local skin friction coefficient and the local Nusselt number have been depicted for a variety of pertinent parameters.

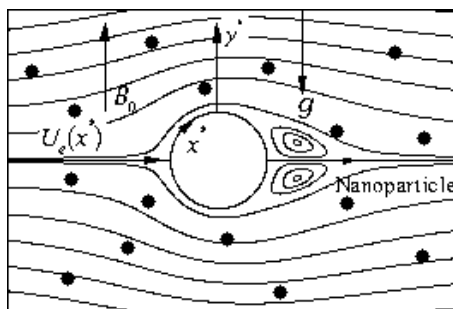


Fig. 1. Physical model and coordinate system



Table 1. Thermophysical properties of water, Cu and Al₂O₃ [18]

	C_p (J/kgK)	ρ (kg/m ³)	κ (W/m K)	$\beta \times 10^{-5}$ (1/K)	σ (Ω m) ⁻¹
Water	4179	997.1	0.613	21	0.05
Cu	385	8933	400	1.67	5.96×10^7
Al ₂ O ₃	765	3970	40	0.85	3.69×10^7

2. Framework of the Model

We take into account an unsteady, combined free-forced convective boundary layer flow of a hybrid nanofluid past a heated cylinder. The physical model and an appropriate coordinate system are represented in Fig. 1. Presuming the thermophysical properties of hybrid nanofluid as constants, they are given in Table 1. Under Boussinesq assumptions, the set of governing equations for a hybrid nanofluid, as rendered in [3, 5, 24, 37, 38], is

$$\frac{\partial u^*}{\partial x^*} + \frac{\partial v^*}{\partial y^*} = 0, \quad (1)$$

$$\frac{\partial u^*}{\partial t^*} + u^* \frac{\partial u^*}{\partial x^*} + v^* \frac{\partial u^*}{\partial y^*} = U_e \frac{dU_e}{dx^*} + \frac{\mu_{hnf}}{\rho_{hnf}} \frac{\partial^2 u^*}{\partial y^{*2}} + \frac{(\rho\beta)_{hnf}}{\rho_{hnf}} g(T - T_\infty) \sin\left(\frac{x^*}{r}\right) - \frac{\sigma_{hnf} B_0^2}{\rho_{hnf}} (u^* - U_e), \quad (2)$$

$$\frac{\partial T}{\partial t^*} + u^* \frac{\partial T}{\partial x^*} + v^* \frac{\partial T}{\partial y^*} = \alpha_{hnf} \frac{\partial^2 T}{\partial y^{*2}} - \frac{1}{(\rho C)_{hnf}} \frac{\partial q_r}{\partial y^*}, \quad (3)$$

where x^* and y^* measure the distances along and normal to the surface of the cylinder, u^* and v^* are velocities along x^* and y^* respectively, r denotes the radius of circular cylinder, T and T_∞ stand for the temperature of the hybrid fluid and ambient temperature, g is the acceleration due to gravity, B_0 is the magnetic field acting in normal direction to the surface of the cylinder and t^* corresponds to the time.

The associated boundary conditions are

$$\begin{aligned} u^* = v^* = 0, T = T_w \quad \text{at } y^* = 0, \\ u^* = U_e(x^*), T = T_\infty \quad \text{as } y^* \rightarrow \infty, \end{aligned} \quad (4)$$

where $U_e(x^*) = U_\infty \sin(x^*/r)$ is the boundary edge velocity.

The physical quantities μ_{hnf} and ρ_{hnf} are defined as [24]:

$$\mu_{hnf} = \frac{\mu_f}{\left(1 - (\phi_{np_1} + \phi_{np_2})\right)^{2.5}}, \quad \rho_{hnf} = \phi_{np_1} \rho_{np_1} + \phi_{np_2} \rho_{np_2} + (1 - \phi_{hnf}) \rho_f, \quad \phi_{hnf} = \phi_{np_1} + \phi_{np_2}. \quad (5)$$

The terms ϕ_{np_1} and ϕ_{np_2} are the volume fractions of nanoparticles respectively.

Additional physical properties α_{hnf} , $(\rho C)_{hnf}$ and κ_{hnf} correspond to the thermal diffusivity, heat capacity and thermal conductivity of hybrid nanofluid which are defined as [24]:

$$\alpha_{hnf} = \frac{\kappa_{hnf}}{(\rho C)_{hnf}}, \quad (\rho C)_{hnf} = \phi_{np_1} (\rho C)_{np_1} + \phi_{np_2} (\rho C)_{np_2} + (1 - \phi_{hnf}) (\rho C)_f, \quad (6)$$

$$\frac{\kappa_{hnf}}{\kappa_f} = \frac{(\kappa_{hp} + 2\kappa_f) - 2\phi_{hnf}(\kappa_f - \kappa_{hp})}{(\kappa_{hp} + 2\kappa_f) + \phi_{hnf}(\kappa_f - \kappa_{hp})}, \quad \kappa_{hp} = \frac{\phi_{np_1} \kappa_{np_1} + \phi_{np_2} \kappa_{np_2}}{\phi_{np_1} + \phi_{np_2}}, \quad (7)$$

The heat flux term attributed to radiation q_r in Eq. (3) is generalized using Rosseland approximation [39] and can be demonstrated as

$$q_r = -\frac{4\tilde{\sigma}}{3\tilde{a}} \frac{\partial T^4}{\partial y^*}, \quad (8)$$

where $\tilde{\sigma}$ refers to the Stefan-Boltzman constant and \tilde{a} corresponds to the coefficient of mean absorption.

In addition, the constants σ_{hnf} and $(\rho\beta)_{hnf}$ are the effective electrical conductivity and coefficient of volumetric expansion for hybrid nanofluid and are defined as [24]:

$$\frac{\sigma_{hnf}}{\sigma_f} = \frac{(\sigma_{hp} + 2\sigma_f) - 2\phi_{hnf}(\sigma_f - \sigma_{hp})}{(\sigma_{hp} + 2\sigma_f) + \phi_{hnf}(\sigma_f - \sigma_{hp})}, \quad \sigma_{hp} = \frac{\phi_{np_1} \sigma_{np_1} + \phi_{np_2} \sigma_{np_2}}{\phi_{np_1} + \phi_{np_2}}, \quad (9)$$

$$(\rho\beta)_{hnf} = \phi_{np_1} (\rho\beta)_{np_1} + \phi_{np_2} (\rho\beta)_{np_2} + (1 - \phi_{hnf}) (\rho\beta)_f, \quad (10)$$

The physical properties μ_f , ρ_f , σ_f , α_f and κ_f are dynamic viscosity, density, electrical conductivity, thermal diffusivity and thermal conductivity of the base fluid respectively.



To make the leading equations (1)-(3) into non-dimensional form, let us address the transformation as follows:

$$X = \frac{x^*}{r}, Y = \text{Re}^{1/2} \frac{y^*}{r}, U = \frac{u^*}{U_\infty}, V = \frac{\text{Re}^{1/2} v^*}{U_\infty}, \xi = \frac{U_\infty t^*}{r}, \theta = \frac{T - T_\infty}{T_w - T_\infty}, \quad (11)$$

where $\text{Re} = U_\infty r / \nu_f$ represents the Reynolds number. Therefore we have

$$\frac{\partial U}{\partial X} + \frac{\partial V}{\partial Y} = 0, \quad (12)$$

$$\frac{\partial U}{\partial \xi} + U \frac{\partial U}{\partial X} + V \frac{\partial U}{\partial Y} = \frac{\mu_{\text{hnf}}}{\mu_f} \frac{\rho_f}{\rho_{\text{hnf}}} \frac{\partial^2 U}{\partial Y^2} + \text{Ri} \frac{(\rho\beta)_{\text{hnf}}}{(\rho\beta)_f} \frac{\rho_f}{\rho_{\text{hnf}}} \theta \sin X + \sin X \cos X - M \frac{\sigma_{\text{hnf}}}{\sigma_f} \frac{\rho_f}{\rho_{\text{hnf}}} (U - \sin X), \quad (13)$$

$$\frac{\partial \theta}{\partial \xi} + U \frac{\partial \theta}{\partial X} + V \frac{\partial \theta}{\partial Y} = \frac{1}{\text{Pr}} \frac{\alpha_{\text{hnf}}}{\alpha_f} \left\{ 1 + \frac{4}{3} \frac{\kappa_f}{\kappa_{\text{hnf}}} \text{R}_d (1 + \Delta \theta)^3 \right\} \frac{\partial^2 \theta}{\partial Y^2} + 4 \frac{1}{\text{Pr}} \frac{(\rho C)_f}{(\rho C)_{\text{hnf}}} \Delta \text{R}_d (1 + \Delta \theta)^2 \theta'^2, \quad (14)$$

along with

$$\begin{aligned} Y = 0 : U = V = 0, \theta = 1, \\ Y \rightarrow \infty : U = U_e(X), \theta = 0, \end{aligned} \quad (15)$$

where Pr , Ri , Gr , M , R_d and Δ are addressed as the Prandtl number, mixed convection parameter, Grashof number, magnetic field parameter, radiation-conduction parameter and surface temperature parameter consecutively and are defined by

$$\text{Pr} = \frac{\mu_f}{\rho_f \alpha_f}, \text{Ri} = \frac{\text{Gr}}{\text{Re}^2}, \text{Gr} = \frac{g \beta_f (T_w - T_\infty) r^3 \rho_f^2}{\mu_f^2}, M = \frac{\sigma_f B_0^2 r}{\rho_f U_\infty}, \text{R}_d = \frac{4 \sigma T_\infty^3}{a k_f}, \Delta = \frac{T_w}{T_\infty} - 1. \quad (16)$$

3. Solution Methodologies

3.1 Formulation using stream function

In order to integrate the equations (13)-(14) numerically, let us first convert them into suitable form using the following set of transformations

$$\psi = (1 - e^{-\xi})^{1/2} \sin X F(\xi, \eta, X), \eta = (1 - e^{-\xi})^{-1/2} Y, \theta(\xi, Y, X) = \theta(\xi, \eta, X), \quad (17)$$

where η is a similarity variable, ψ stands for stream function and F is dimensionless stream function. It is noted that similar transformations are introduced by Awang and Riley [40] which are valid for small time and Roy et al. [41] which are valid for all time.

In terms of ψ two velocity components U and V are expressed in the following form

$$U = \frac{\partial \psi}{\partial Y}, V = -\frac{\partial \psi}{\partial X}. \quad (18)$$

By applying above transformations into the Eqs. (13)-(14), we find

$$\begin{aligned} \frac{\mu_{\text{hnf}}}{\mu_f} \frac{\rho_f}{\rho_{\text{hnf}}} F''' + \frac{1}{2} e^{-\xi} \eta F'' + (1 - e^{-\xi}) \cos X (FF'' - F'^2) + (1 - e^{-\xi}) \cos X + \text{Ri} \frac{(\rho\beta)_{\text{hnf}}}{(\rho\beta)_f} \frac{\rho_f}{\rho_{\text{hnf}}} (1 - e^{-\xi}) \theta \\ - M \frac{\sigma_{\text{hnf}}}{\sigma_f} \frac{\rho_f}{\rho_{\text{hnf}}} (1 - e^{-\xi}) (F' - 1) = (1 - e^{-\xi}) \frac{\partial F'}{\partial \xi} + (1 - e^{-\xi}) \sin X \left(F' \frac{\partial F'}{\partial X} - F'' \frac{\partial F}{\partial X} \right), \end{aligned} \quad (19)$$

$$\begin{aligned} \frac{1}{\text{Pr}} \frac{\alpha_{\text{hnf}}}{\alpha_f} \left\{ 1 + \frac{4}{3} \frac{\kappa_f}{\kappa_{\text{hnf}}} \text{R}_d (1 + \Delta \theta)^3 \right\} \theta'' + 4 \frac{1}{\text{Pr}} \frac{(\rho C)_f}{(\rho C)_{\text{hnf}}} \Delta \text{R}_d (1 + \Delta \theta)^2 \theta'^2 + \frac{1}{2} e^{-\xi} \eta \theta' + (1 - e^{-\xi}) \cos X F \theta' \\ = (1 - e^{-\xi}) \frac{\partial \theta}{\partial \xi} + (1 - e^{-\xi}) \sin X \left(F' \frac{\partial \theta}{\partial X} - \theta' \frac{\partial F}{\partial X} \right), \end{aligned} \quad (20)$$

with boundary conditions

$$\begin{aligned} F(\xi, 0, X) = 0, F'(\xi, 0, X) = 0, \theta(\xi, 0, X) = 1, \\ F'(\xi, \infty, X) = 1, \theta(\xi, \infty, X) = 0. \end{aligned} \quad (21)$$

In fluid dynamics, two important physical properties are local skin friction coefficient, C_f , and local Nusselt number, Nu , and they are expressed as

$$C_f = \frac{2 \mu_{\text{hnf}}}{\rho_f U_\infty^2} \left(\frac{\partial u^*}{\partial y^*} \right)_{y^*=0}, \quad (22)$$



$$Nu = -\frac{\kappa_{hmf} T}{\kappa_f (T_w - T_\infty)} \left(\frac{\partial T}{\partial y^*} \right)_{y^*=0}. \quad (23)$$

Upon substitution of the relation (11) and (17) into Eqs. (22) and (23) we have,

$$\frac{1}{2} Re^{1/2} C_f = \frac{\mu_{hmf}}{\mu_f} (1 - e^{-\xi})^{-1/2} \sin X F''(\xi, 0, X), \quad (24)$$

$$Re^{-1/2} Nu = -\frac{\kappa_{hmf}}{\kappa_f} (1 - e^{-\xi})^{-1/2} \theta'(\xi, 0, X). \quad (25)$$

3.1.1 Numerical method for all time period

With a view to utilizing the procedure of finite difference to solve the partial differential Eqs. (19)-(21), we first convert them into the second order differential equations by assuming,

$$F' = u, F = v \quad (26)$$

Replacing the Eq. (26) into the Eqs. (19)-(20), we find

$$\frac{\mu_{hmf}}{\mu_f} \frac{\rho_f}{\rho_{hmf}} u'' + \frac{1}{2} d_1 \eta u' + d_2 \cos X (v u' - u^2) + d_2 \cos X + Ri \frac{(\rho\beta)_{hmf}}{(\rho\beta)_f} \frac{\rho_f}{\rho_{hmf}} d_2 \theta - M \frac{\sigma_{hmf}}{\sigma_f} \frac{\rho_f}{\rho_{hmf}} d_2 (u - 1) = d_2 \frac{\partial u}{\partial \xi} + d_2 \sin X \left(u \frac{\partial u}{\partial X} - u' \frac{\partial v}{\partial X} \right), \quad (27)$$

$$\frac{1}{Pr} \frac{\alpha_{hmf}}{\alpha_f} \left\{ 1 + \frac{4}{3} \frac{\kappa_f}{\kappa_{hmf}} R_d (1 + \Delta\theta)^3 \right\} \theta'' + 4 \frac{1}{Pr} \frac{(\rho C)_f}{(\rho C)_{hmf}} \Delta R_d (1 + \Delta\theta)^2 \theta'^2 + \frac{1}{2} d_1 \eta \theta' + d_2 \cos X F \theta' = d_2 \frac{\partial \theta}{\partial \xi} + d_2 \sin X \left(F' \frac{\partial \theta}{\partial X} - \theta' \frac{\partial F}{\partial X} \right), \quad (28)$$

along with the boundary conditions

$$\begin{aligned} v(\xi, 0, X) &= 0, u(\xi, 0, X) = 0, \theta(\xi, 0, X) = 1, \\ u(\xi, \infty, X) &= 1, \theta(\xi, \infty, X) = 0. \end{aligned} \quad (29)$$

In these above equations, we surmise

$$d_1 = e^{-\xi}, d_2 = (1 - e^{-\xi}). \quad (30)$$

Now the system of equations (27)-(28) are decoded using central difference technique along η direction while backward difference approximation has been used along X and ξ directions. Hence, the system of tridiagonal algebraic equations is formed as:

$$B_k S_{i,j-1}^n + A_k S_{i,j}^n + C_k S_{i,j+1}^n = D_k \quad (31)$$

Here, the grid points used in X and η directions are denoted by i and j where i, j varies from 1 to M and 1 to N respectively. Also, the superscript n is utilized to illustrate grid points in ξ direction where n varies from 1 to K . Moreover, U is represented by the subscript $k = 1$ while θ stands for $k = 2$.

Now the coefficients A_k, B_k, C_k, D_k obtained from Eqs. (27) and (28) are given as follows:

$$A_1 = 2 \frac{\mu_{hmf}}{\mu_f} \frac{\rho_f}{\rho_{hmf}} + (\Delta\eta)^2 d_2 \left\{ \left(\cos X + \frac{\sin X}{\Delta X} \right) u_{2,j}^n + \frac{1}{\Delta\xi} + M \frac{\sigma_{hmf}}{\sigma_f} \frac{\rho_f}{\rho_{hmf}} \right\}, \quad (32)$$

$$B_1 = -\frac{\mu_{hmf}}{\mu_f} \frac{\rho_f}{\rho_{hmf}} - \frac{\Delta\eta}{2} \left\{ \frac{d_1}{2} \left(\frac{\eta_j + \eta_{j-1}}{2} \right) + d_2 \left(\cos X v_{2,j}^n + \sin X \frac{v_{2,j}^n - v_{1,j}^n}{\Delta X} \right) \right\}, \quad (33)$$

$$C_1 = -\frac{\mu_{hmf}}{\mu_f} \frac{\rho_f}{\rho_{hmf}} + \frac{\Delta\eta}{2} \left\{ \frac{d_1}{2} \left(\frac{\eta_j + \eta_{j-1}}{2} \right) + d_2 \left(\cos X v_{2,j}^n + \sin X \frac{v_{2,j}^n - v_{1,j}^n}{\Delta X} \right) \right\}, \quad (34)$$

$$D_1 = (\Delta\eta)^2 d_2 \left\{ \frac{u_{2,j}^{n-1}}{\Delta\xi} + \sin X \frac{u_{2,j}^n u_{1,j}^n}{\Delta X} + \left(\cos X + Ri \frac{(\rho\beta)_{hmf}}{(\rho\beta)_f} \frac{\rho_f}{\rho_{hmf}} \theta_{2,j}^n + M \frac{\sigma_{hmf}}{\sigma_f} \frac{\rho_f}{\rho_{hmf}} \right) \right\}, \quad (35)$$

$$A_2 = 2 \frac{1}{Pr} \frac{\alpha_{hmf}}{\alpha_f} \left\{ 1 + \frac{4}{3} \frac{\kappa_f}{\kappa_{hmf}} R_d (1 + \Delta\theta)^3 \right\} + (\Delta\eta)^2 \frac{d_2}{\Delta\xi} + (\Delta\eta)^2 d_2 \sin X \frac{u_{2,j}^n}{\Delta X}, \quad (36)$$

$$B_2 = -\frac{1}{Pr} \frac{\alpha_{hmf}}{\alpha_f} \left\{ 1 + \frac{4}{3} \frac{\kappa_f}{\kappa_{hmf}} R_d (1 + \Delta\theta)^3 \right\} - \frac{\Delta\eta}{2} \left\{ 4 \frac{1}{Pr} \frac{(\rho C)_f}{(\rho C)_{hmf}} R_d \Delta (1 + \Delta\theta)^2 \frac{\theta_{2,j+1}^n - \theta_{2,j-1}^n}{2\Delta\eta} + \frac{1}{2} d_1 \eta + d_2 \cos X v_{2,j}^n + d_2 \sin X \frac{v_{2,j}^n - v_{1,j}^n}{\Delta X} \right\}, \quad (37)$$



$$C_2 = -\frac{1}{\text{Pr}} \frac{\alpha_{\text{hnf}}}{\alpha_f} \left\{ 1 + \frac{4}{3} \frac{\kappa_f}{\kappa_{\text{hnf}}} R_d (1 + \Delta\theta)^3 \right\} + \frac{\Delta\eta}{2} \left\{ 4 \frac{1}{\text{Pr}} \frac{(\rho C)_f}{(\rho C)_{\text{hnf}}} \Delta R_d (1 + \Delta\theta)^2 \frac{\theta_{2,j+1}^n - \theta_{2,j-1}^n}{2\Delta\eta} + \frac{1}{2} d_1 \eta + d_2 \cos X v_{2,j}^n + d_2 \sin X \frac{v_{2,j}^n - v_{1,j}^n}{\Delta X} \right\}, \quad (38)$$

$$D_2 = (\Delta\eta)^2 d_2 \frac{\theta_{2,j}^{n-1}}{\Delta\xi} + (\Delta\eta)^2 d_2 \sin X u_{2,j}^n \frac{\theta_{1,j}^n}{\Delta X}, \quad (39)$$

where A_1, B_1, C_1, D_1 are regarded as the coefficients of $u_{i,j}^n, u_{i,j-1}^n, u_{i,j+1}^n$ and corresponding right hand side, while the coefficients of $\theta_{i,j}^n, \theta_{i,j-1}^n, \theta_{i,j+1}^n$ and corresponding right hand side are regarded by A_2, B_2, C_2, D_2 .

Here we simulate the tridiagonal Eq. (31) for i by applying Thomas algorithm [42] for specified j, n values. Hence, acquired result is respectively shown along j and n directions. To obtain the numerical solutions, we select the convergence inference in a manner that the difference values of F in two successive iterations are smaller than 10^{-5} . Here X direction is confined within a range 0.0 to π and along η direction no limited range has taken to understand better fluid flow separation. Moreover, the mesh sizes of $\Delta X, \Delta\eta$ and $\Delta\xi$ are taken as $\pi/360, 0.02$ and 0.01 respectively to obtain grid independent solutions.

Now we attain $(\partial u/\partial\eta)_{\eta=0}$ and $(\partial\theta/\partial\eta)_{\eta=0}$ values from the previous solutions to enumerate skin friction coefficient $(1/2)\text{Re}^{1/2}C_f$ and Nusselt number $\text{Re}^{-1/2}\text{Nu}$ as below:

$$\frac{1}{2}\text{Re}^{1/2}C_f = \frac{\mu_{\text{hnf}}}{\mu_f} (1 - e^{-\xi})^{-1/2} \sin X \left(\frac{\partial u}{\partial\eta} \right)_{\eta=0}, \quad (40)$$

$$\text{Re}^{-1/2}\text{Nu} = -\frac{\kappa_{\text{hnf}}}{\kappa_f} (1 - e^{-\xi})^{-1/2} \left(\frac{\partial\theta}{\partial\eta} \right)_{\eta=0}. \quad (41)$$

3.1.2 Perturbation method for short time period ($\xi \ll 1$)

To study short time period, equations (19) and (20) have been simplified to a convenient form at first. When $\xi \ll 1$, let us assume $e^{-\xi} \approx 1, 1 - e^{-\xi} \approx \xi$. Accordingly, equations (19)-(20) are reconstructed into

$$\frac{\mu_{\text{hnf}}}{\mu_f} \frac{\rho_f}{\rho_{\text{hnf}}} F''' + \frac{1}{2} \eta F'' + \xi \cos X (FF'' - F'^2) + \xi \cos X + \text{Ri} \frac{(\rho\beta)_{\text{hnf}}}{(\rho\beta)_f} \frac{\rho_f}{\rho_{\text{hnf}}} \xi \theta - M \frac{\sigma_{\text{hnf}}}{\sigma_f} \frac{\rho_f}{\rho_{\text{hnf}}} \xi (F' - 1) = \xi \frac{\partial F'}{\partial \xi} + \xi \sin X \left(F' \frac{\partial F'}{\partial X} - F'' \frac{\partial F}{\partial X} \right), \quad (42)$$

$$\frac{1}{\text{Pr}} \frac{\alpha_{\text{hnf}}}{\alpha_f} \left\{ 1 + \frac{4}{3} \frac{\kappa_f}{\kappa_{\text{hnf}}} R_d (1 + \Delta\theta)^3 \right\} \theta'' + 4 \frac{1}{\text{Pr}} \frac{(\rho C)_f}{(\rho C)_{\text{hnf}}} \Delta R_d (1 + \Delta\theta)^2 \theta'^2 + \frac{1}{2} \eta \theta' + \xi \cos X F \theta' = \xi \frac{\partial \theta}{\partial \xi} + \xi \sin X \left(F' \frac{\partial \theta}{\partial X} - \theta' \frac{\partial F}{\partial X} \right), \quad (43)$$

with

$$\begin{aligned} F(\xi, 0, X) &= 0, F'(\xi, 0, X) = 0, \theta(\xi, 0, X) = 1, \\ F'(\xi, \infty, X) &= 1, \theta(\xi, \infty, X) = 0. \end{aligned} \quad (44)$$

For $\xi \ll 1$, the consequent equations are found by expanding F and θ in powers of ξ as below

$$F = \sum_{l=0}^{\infty} \xi^l F_l \quad \text{and} \quad \theta = \sum_{l=0}^{\infty} \xi^l \theta_l \quad (45)$$

Putting the expressions of Eq. (45) into (42)-(43) and then equating corresponding ξ coefficients up to the order two, we find system of equations for $O(\xi^0)$:

$$\frac{\mu_{\text{hnf}}}{\mu_f} \frac{\rho_f}{\rho_{\text{hnf}}} F_0''' + \frac{1}{2} \eta F_0'' = 0, \quad (46)$$

$$\frac{1}{\text{Pr}} \frac{\alpha_{\text{hnf}}}{\alpha_f} \left\{ 1 + \frac{4}{3} \frac{\kappa_f}{\kappa_{\text{hnf}}} R_d (1 + \Delta\theta_0)^3 \right\} \theta_0'' + 4 \frac{1}{\text{Pr}} \frac{(\rho C)_f}{(\rho C)_{\text{hnf}}} \Delta R_d (1 + \Delta\theta_0)^2 \Delta\theta_0'^2 + \frac{1}{2} \eta \theta_0' = 0, \quad (47)$$

$$\begin{aligned} F_0(0, X) &= 0, F_0'(0, X) = 0, \theta_0(0, X) = 1, \\ F_0'(\infty, X) &= 1, \theta_0(\infty, X) = 0 \end{aligned} \quad (48)$$

System of equations for $O(\xi^1)$:

$$\frac{\mu_{\text{hnf}}}{\mu_f} \frac{\rho_f}{\rho_{\text{hnf}}} F_1''' + \left(\frac{1}{2} \eta F_1'' - F_1' - M \frac{\sigma_{\text{hnf}}}{\sigma_f} \frac{\rho_f}{\rho_{\text{hnf}}} F_0' \right) + \cos X (F_0 F_0'' - F_0'^2) + \cos X + \text{Ri} \frac{(\rho\beta)_{\text{hnf}}}{(\rho\beta)_f} \frac{\rho_f}{\rho_{\text{hnf}}} \theta_0 + M \frac{\sigma_{\text{hnf}}}{\sigma_f} \frac{\rho_f}{\rho_{\text{hnf}}} - \sin X \left(F_0' \frac{\partial F_0'}{\partial X} - F_0'' \frac{\partial F_0}{\partial X} \right) = 0, \quad (49)$$

$$\begin{aligned} &\frac{1}{\text{Pr}} \frac{\alpha_{\text{hnf}}}{\alpha_f} \left\{ 1 + \frac{4}{3} \frac{\kappa_f}{\kappa_{\text{hnf}}} R_d (1 + \Delta\theta_0)^3 \right\} \theta_1'' + 4 \frac{1}{\text{Pr}} \frac{(\rho C)_f}{(\rho C)_{\text{hnf}}} \Delta R_d (1 + \Delta\theta_0)^2 \theta_0'' \theta_1 + 8 \frac{1}{\text{Pr}} \frac{(\rho C)_f}{(\rho C)_{\text{hnf}}} \Delta R_d \theta_0' (1 + \Delta\theta_0) \left(\Delta\theta_0' \theta_1 + \theta_1' (1 + \Delta\theta_0) \right) \\ &+ \frac{1}{2} \eta \theta_1' + \cos X F_0 \theta_0' - \theta_1 - \sin X \left(F_0' \frac{\partial \theta_0}{\partial X} - \theta_0' \frac{\partial F_0}{\partial X} \right) = 0, \end{aligned} \quad (50)$$



$$\begin{aligned} F_1(0, X) = 0, F_1'(0, X) = 0, \theta_1(0, X) = 0, \\ F_1'(\infty, X) = 0, \theta_1(\infty, X) = 0. \end{aligned} \quad (51)$$

System of equations for $O(\xi^2)$:

$$\begin{aligned} \frac{\mu_{hmf}}{\mu_f} \frac{\rho_f}{\rho_{hmf}} F_2''' + \frac{1}{2} \eta F_2'' - 2F_2' - M \frac{\sigma_{hmf}}{\sigma_f} \frac{\rho_f}{\rho_{hmf}} F_1' + \cos X (F_0 F_1'' + F_1 F_0'' - 2F_0' F_1') + Ri \frac{(\rho\beta)_{hmf}}{(\rho\beta)_f} \frac{\rho_f}{\rho_{hmf}} \theta_1 \\ - \sin X \left(F_0' \frac{\partial F_1'}{\partial X} + F_1' \frac{\partial F_0'}{\partial X} - F_0'' \frac{\partial F_1}{\partial X} - F_1'' \frac{\partial F_0}{\partial X} \right) = 0, \end{aligned} \quad (52)$$

$$\begin{aligned} \frac{1}{Pr} \frac{\alpha_{hmf}}{\alpha_f} \left\{ 1 + \frac{4}{3} \frac{\kappa_f}{\kappa_{hmf}} R_d (1 + \Delta\theta_0)^3 \right\} \theta_2'' + 4 \frac{1}{Pr} \frac{(\rho C)_f}{(\rho C)_{hmf}} R_d \theta_1 (1 + \Delta\theta_0) \left\{ \theta_1'' (1 + \Delta\theta_0) + \theta_1 \theta_0'' \right\} \\ + 4 \frac{1}{Pr} \frac{(\rho C)_f}{(\rho C)_{hmf}} R_d \Delta\theta_1' (1 + \Delta\theta_0) \left\{ 4\Delta\theta_0' \theta_1 + \theta_1' (1 + \Delta\theta_0) \right\} + 4 \frac{1}{Pr} \frac{(\rho C)_f}{(\rho C)_{hmf}} \Delta^3 R_d \theta_0'^2 \theta_1'^2 \\ + \cos X (F_0 \theta_1' + F_1 \theta_0') + \frac{1}{2} \eta \theta_2' - 2\theta_2 - \sin X \left(F_0' \frac{\partial \theta_1}{\partial X} + F_1' \frac{\partial \theta_0}{\partial X} - \theta_0' \frac{\partial F_1}{\partial X} - \theta_1' \frac{\partial F_0}{\partial X} \right) = 0, \end{aligned} \quad (53)$$

$$\begin{aligned} F_2(0, X) = 0, F_2'(0, X) = 0, \theta_2(0, X) = 0, \\ F_2'(\infty, X) = 0, \theta_2(\infty, X) = 0. \end{aligned} \quad (54)$$

In above equations, the differentiation is denoted by prime regarding η . We use implicit Runge-Kutta-Butcher procedure [43] with iteration procedure of Nachtsheim and Swigert [44] to obtain the solution of above equations. Values of $F_l'(0, X)$ and $\theta_l'(0, X)$ are attained for $l = 0, 1$ and 2 . Then $(1/2)Re^{1/2}C_f$ and $Re^{-1/2}Nu$ are found easily by

$$\frac{1}{2} Re^{1/2} C_f = \frac{\mu_{hmf}}{\mu_f} (1 - e^{-\xi})^{-1/2} \sin X \sum_{l=0}^{\infty} \xi^l F_l', \quad (55)$$

$$Re^{-1/2} Nu = - \frac{\kappa_{hmf}}{\kappa_f} (1 - e^{-\xi})^{-1/2} \sum_{l=0}^{\infty} \xi^l \theta_l'. \quad (56)$$

3.1.3 Asymptotic method for long time period ($\xi \gg 1$)

In order to obtain the solutions of equations (19)-(20) for long time period, here the time considered as $\xi \ll 1$. For $\xi \ll 1$, we assume $e^{-\xi} \approx \xi^{-1}$, $1 - e^{-\xi} \approx 1 - \xi^{-1}$. Hence, the equations (19) and (20) are remodeled into following set of equations,

$$\begin{aligned} \frac{\mu_{hmf}}{\mu_f} \frac{\rho_f}{\rho_{hmf}} F''' + \frac{1}{2} \xi^{-1} \eta F'' + (1 - \xi^{-1}) \cos X (FF'' - F'^2) + (1 - \xi^{-1}) \cos X + Ri \frac{(\rho\beta)_{hmf}}{(\rho\beta)_f} \frac{\rho_f}{\rho_{hmf}} (1 - \xi^{-1}) \theta - M \frac{\sigma_{hmf}}{\sigma_f} \frac{\rho_f}{\rho_{hmf}} (1 - \xi^{-1}) (F' - 1) \\ = (1 - \xi^{-1}) \frac{\partial F'}{\partial \xi} + (1 - \xi^{-1}) \sin X \left(F' \frac{\partial F'}{\partial X} - F'' \frac{\partial F}{\partial X} \right), \end{aligned} \quad (57)$$

$$\begin{aligned} \frac{1}{Pr} \frac{\alpha_{hmf}}{\alpha_f} \left\{ 1 + \frac{4}{3} \frac{\kappa_f}{\kappa_{hmf}} R_d (1 + \Delta\theta)^3 \right\} \theta'' + 4 \frac{1}{Pr} \frac{(\rho C)_f}{(\rho C)_{hmf}} \Delta R_d (1 + \Delta\theta)^2 \theta'^2 + \frac{1}{2} \xi^{-1} \eta \theta' + (1 - \xi^{-1}) \cos X F \theta' \\ = (1 - \xi^{-1}) \frac{\partial \theta}{\partial \xi} + (1 - \xi^{-1}) \sin X \left(F' \frac{\partial \theta}{\partial X} - \theta' \frac{\partial F}{\partial X} \right), \end{aligned} \quad (58)$$

where

$$\begin{aligned} F(\xi, 0, X) = 0, F'(\xi, 0, X) = 0, \theta(\xi, 0, X) = 1, \\ F'(\xi, \infty, X) = 1, \theta(\xi, \infty, X) = 0. \end{aligned} \quad (59)$$

Now we expand F and θ using the expressions below

$$F = \sum_{l=0}^{\infty} \xi^{-l} F_l \quad \text{and} \quad \theta = \sum_{l=0}^{\infty} \xi^{-l} \theta_l. \quad (60)$$

Combining the equations (60) with (57) and (58), we conclude the coefficients of ξ^0 as

$$\frac{\mu_{hmf}}{\mu_f} \frac{\rho_f}{\rho_{hmf}} F_0''' + \cos X (F_0 F_0'' - F_0'^2) + \cos X + Ri \frac{(\rho\beta)_{hmf}}{(\rho\beta)_f} \frac{\rho_f}{\rho_{hmf}} \theta_0 - M \frac{\sigma_{hmf}}{\sigma_f} \frac{\rho_f}{\rho_{hmf}} (F_0' - 1) = \sin X \left(F_0' \frac{\partial F_0'}{\partial X} - F_0'' \frac{\partial F_0}{\partial X} \right) \quad (61)$$

$$\frac{1}{Pr} \frac{\alpha_{hmf}}{\alpha_f} \left\{ 1 + \frac{4}{3} \frac{\kappa_f}{\kappa_{hmf}} R_d (1 + \Delta\theta_0)^3 \right\} \theta_0'' + 4 \frac{1}{Pr} \frac{(\rho C)_f}{(\rho C)_{hmf}} \Delta R_d (1 + \Delta\theta_0)^2 \theta_0'^2 + \cos X F_0 \theta_0' = \sin X \left(F_0' \frac{\partial \theta_0}{\partial X} - \theta_0' \frac{\partial F_0}{\partial X} \right) \quad (62)$$



with boundary conditions

$$\begin{aligned} F_0(0, X) = 0, F_0'(0, X) = 0, \theta_0(0, X) = 1, \\ F_0'(\infty, X) = 1, \theta_0(\infty, X) = 0. \end{aligned} \quad (63)$$

We implement local non-similarity technique [43] to simplify coupled equations (57)-(58) and then rephrase the equations using the following transformations,

$$\frac{\partial F_0}{\partial X} = b, \frac{\partial F_0'}{\partial X} = b', \frac{\partial \theta_0}{\partial X} = \varphi. \quad (64)$$

Hence the equations (61)-(62) convert into the following form,

$$\frac{\mu_{hnf}}{\mu_f} \frac{\rho_f}{\rho_{hnf}} F_0''' + \cos X (F_0 F_0'' - F_0'^2) + \cos X + \text{Ri} \frac{(\rho\beta)_{hnf}}{(\rho\beta)_f} \frac{\rho_f}{\rho_{hnf}} \theta_0 - \text{M} \frac{\sigma_{hnf}}{\sigma_f} \frac{\rho_f}{\rho_{hnf}} (F_0' - 1) = \sin X (F_0' b' - F_0'' b), \quad (65)$$

$$\frac{1}{\text{Pr}} \frac{\alpha_{hnf}}{\alpha_f} \left\{ 1 + \frac{4}{3} \frac{\kappa_f}{\kappa_{hnf}} R_d (1 + \Delta\theta_0)^3 \right\} \theta_0'' + 4 \frac{1}{\text{Pr}} \frac{(\rho C)_f}{(\rho C)_{hnf}} \Delta R_d (1 + \Delta\theta_0)^2 \theta_0'^2 + \cos X F_0 \theta_0' = \sin X (F_0' \varphi - \theta_0' b). \quad (66)$$

Therefore, resulting boundary conditions imply that,

$$\begin{aligned} F_0(0, X) = 0, F_0'(0, X) = 0, \theta_0(0, X) = 1, \\ F_0'(\infty, X) = 1, \theta_0(\infty, X) = 0. \end{aligned} \quad (67)$$

Now to differentiate the equations (65)-(67) with respect to X , we therefore obtain

$$\begin{aligned} \frac{\mu_{hnf}}{\mu_f} \frac{\rho_f}{\rho_{hnf}} b''' + \cos X (F_0 b'' + b F_0'' - 2 F_0' b') - \sin X - \sin X (F_0 F_0'' - F_0'^2) + \text{Ri} \frac{(\rho\beta)_{hnf}}{(\rho\beta)_f} \frac{\rho_f}{\rho_{hnf}} \varphi - \text{M} \frac{\sigma_{hnf}}{\sigma_f} \frac{\rho_f}{\rho_{hnf}} b' \\ = \sin X (b'^2 - b b'') + \cos X (F_0' b' - F_0'' b), \end{aligned} \quad (68)$$

$$\begin{aligned} \frac{1}{\text{Pr}} \frac{\alpha_{hnf}}{\alpha_f} \left\{ 1 + \frac{4}{3} \frac{\kappa_f}{\kappa_{hnf}} R_d (1 + \Delta\theta_0)^3 \right\} \varphi'' + 4 \frac{1}{\text{Pr}} \frac{(\rho C)_f}{(\rho C)_{hnf}} R_d \theta_0'' (1 + \Delta\theta_0)^2 \Delta\varphi + 8 \frac{1}{\text{Pr}} \frac{(\rho C)_f}{(\rho C)_{hnf}} R_d \left\{ (1 + \Delta\theta_0) \Delta^2 \theta_0'^2 \varphi + (1 + \Delta\theta_0)^2 \Delta\theta_0' \varphi' \right\} \\ + \cos X (F_0 \varphi' + \theta_0' b) - \sin X F_0 \theta_0' = \sin X (b' \varphi - b \varphi') + \cos X (F_0' \varphi - \theta_0' b), \end{aligned} \quad (69)$$

$$\begin{aligned} b'(0, X) = 0, b''(0, X) = 0, \varphi'(0, X) = 0, \\ b''(\infty, X) = 0, \varphi'(\infty, X) = 0. \end{aligned} \quad (70)$$

In order to solve the coupled ordinary differential Eqs. (65)-(70), local non-similarity technique [45] has been used here. Hence $(1/2)\text{Re}^{1/2}C_f$ and $\text{Re}^{-1/2}\text{Nu}$ are attained using the expressions below,

$$\frac{1}{2}\text{Re}^{1/2}C_f = \frac{\mu_{hnf}}{\mu_f} (1 - e^{-\zeta})^{-1/2} \sin X F_0''(0, X) \quad (71)$$

$$\text{Re}^{-1/2}\text{Nu} = -\frac{\kappa_{hnf}}{\kappa_f} (1 - e^{-\zeta})^{-1/2} \theta_0'(0, X) \quad (72)$$

4. Results and Discussion

To show the validity of present method, a comparison for $(1/2)\text{Re}^{1/2}C_f$ and $\text{Re}^{-1/2}\text{Nu}$ values with Wang and Kleinstreuer [10] solution is presented in Figs. 2(a, b). According to this figure, it is observed that present method solution portrays an excellent agreement with Wang and Kleinstreuer [10] solution when $\text{Ri} = 2.0$ and $\text{Pr} = 10$.

Additionally to show the accuracy of numerical results, a comparison between numerical solutions for all time period with asymptotic solutions for long time period and perturbation solutions for short time period is presented in Figs. 3(a) and 3(b). It is clear that $(1/2)\text{Re}^{1/2}C_f$ and $\text{Re}^{-1/2}\text{Nu}$ predicted by numerical simulation yield an excellent agreement with the series solutions.

4.1 Effects of parameters on streamlines and isotherms

Before starting the discussion of the results, it is worthy of mentioning that the boundary layer separation from the surface of the cylinder is defined by $\partial u/\partial y = 0$ at $y^* = 0$ following Schlichting and Gersten [46]. The point of separation (say, S_p) is measured away from the front stagnation point $x^* = 0$. So, the delay or acceleration of boundary layer separation indicates the longer or shorter angular distance ($\leq \pi$) calculated by the definition $\partial u/\partial y = 0$ at $y^* = 0$. For example, if the values of a parameter are R_1, R_2 and R_3 with $R_1 < R_2 < R_3$ and the corresponding points of separation are S_{p1}, S_{p2} and S_{p3} with $S_{p1} < S_{p2} < S_{p3}$, then it will be reported that the increase of the parameter delays the boundary layer separation.



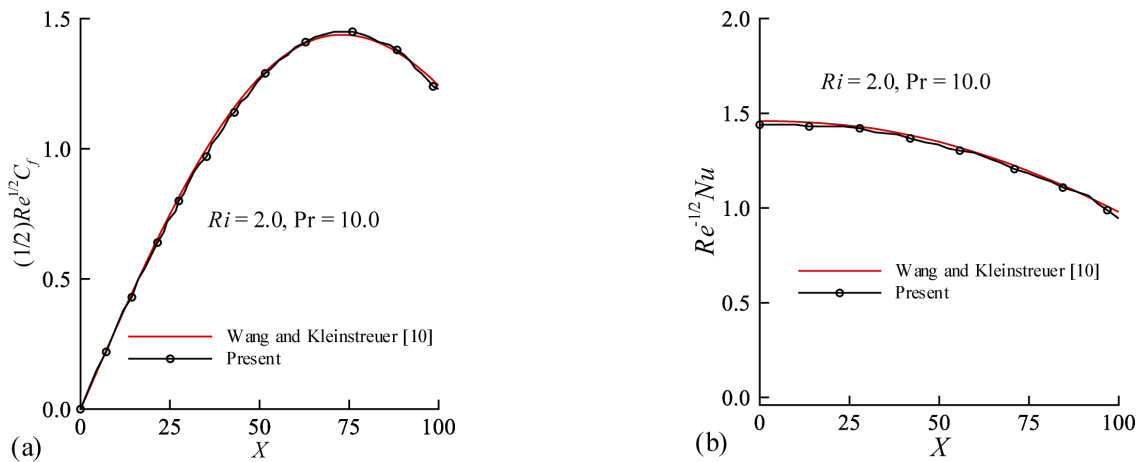


Fig. 2. Comparison of present method and Wang and Kleinstreuer [10] for (a) skin friction coefficient and (b) Nusselt number when $Ri=2.0$, $R_d=0.0$, $\Delta=0.0$, $M=0.0$, $\phi_1=0.0$, $\phi_2=0.0$.

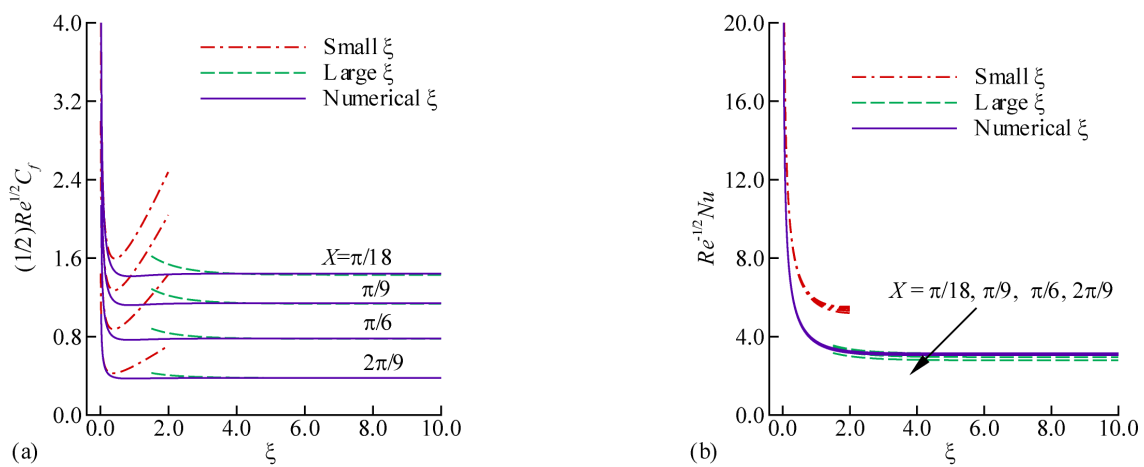


Fig. 3. Comparison of numerical and series solution of (a) skin friction coefficient and (b) Nusselt number when $Ri=1.0$, $R_d=0.5$, $\Delta=0.5$, $M=0.1$, $\phi_1=0.1$, $\phi_2=0.05$.

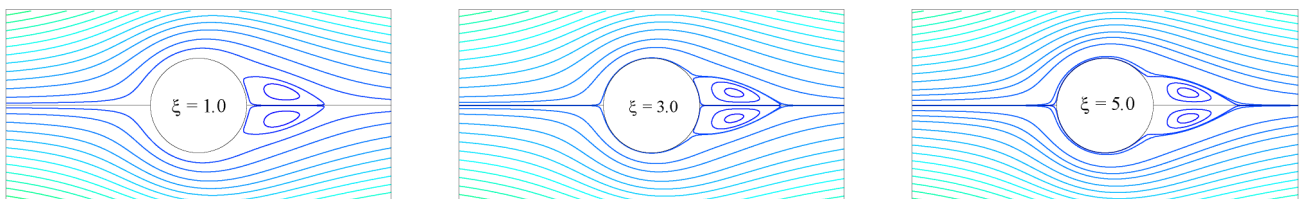


Fig. 4. Streamlines for $Ri=0.1$, $R_d=0.5$, $\Delta=0.5$, $M=0.1$, $\phi_1=0.1$, $\phi_2=0.05$ for varying time ξ .

Figures 4 and 5 illustrate the streamlines and isotherms for varying time, ξ . We observe that vortex area behind the cylinder extends constantly for increased ξ values. Here we take the values of $\xi = 1.0$, 3.0 and 5.0 to show the distinct vortex sizes until the arrival of steady state. After a certain period of time, vortices remain almost same, that is, for $\xi = 3.0$ and 5.0 and therefore we can notice that by reaching the steady state, the flow lines do overlap with each other. When vortex exists behind the cylinder it indicates that the boundary layer separates from the surface and for the steady-state time (i.e., $\xi=5.0$), there are two X -values on the surface of the cylinder so that $\partial u / \partial y = 0$ at $y=0$ i.e., $F''(\xi, 0, X) = 0.0$ (see Ref. [46]). On both sides of the rear stagnation point $X=\pi$, these X -values also correspond to $\psi=0.0$. There is seen reverse flow inside the curve $\psi=0.0$ for which $F''(\xi, 0, X) < 0$ and consequently the vortex bounded by $\psi=0.0$ contains eddies around the line $X=\pi$. Contrary to this phenomenon we find that as time elapses temperature evolves and thermal boundary layer becomes thick. Also the temperature field is elongated in downstream region with time which is identical to the development of vortices with time. The causes are that heat is transferred to the downstream region by forced convection and it is developed around the cylinder by free convection.

Figures 6(a)-(c) and 7(a)-(c) display the effects of Ri on the steady state streamlines and isotherms. It is evident from Figs. 6(a)-(c) that for increased Ri values, the size of vortices becomes smaller persistently and for $Ri=1.0$ vortices disappear. In other words, boundary layer separation accelerates with higher forced convection and it will not take place for mixed convection flow. However, the impact on thermal boundary layer is rather weak for increased Ri . Moreover, with the increase of Ri temperature is distributed in the downstream region. The reason behind the aforesaid characteristics is that the higher flow velocity leads to the reverse flow in the downstream region of the cylinder.



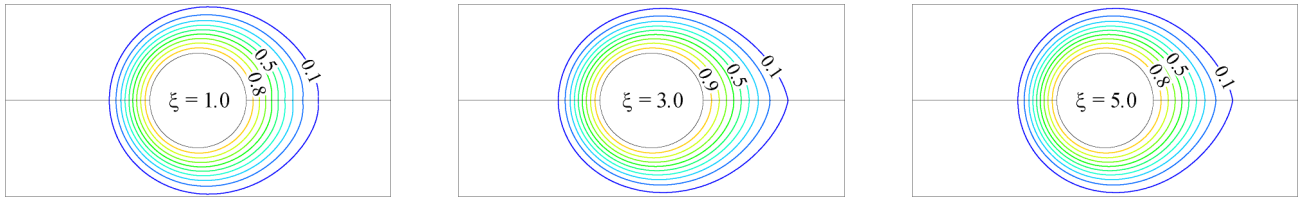


Fig. 5. Isotherms for $Ri=0.1$, $R_d=0.5$, $\Delta=0.5$, $M=0.1$, $\phi_1=0.1$, $\phi_2=0.05$ for varying time ξ .

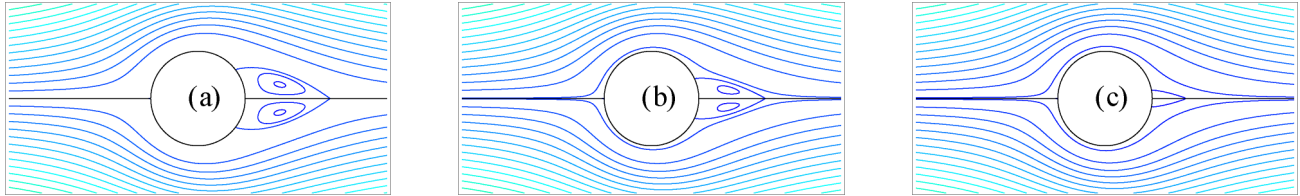


Fig. 6. Streamlines for $R_d=0.5$, $\Delta=0.5$, $M=0.1$, $\phi_1=0.1$, $\phi_2=0.05$ when (a) $Ri=0.0$, (b) $Ri=0.5$, and (c) $Ri=1.0$.

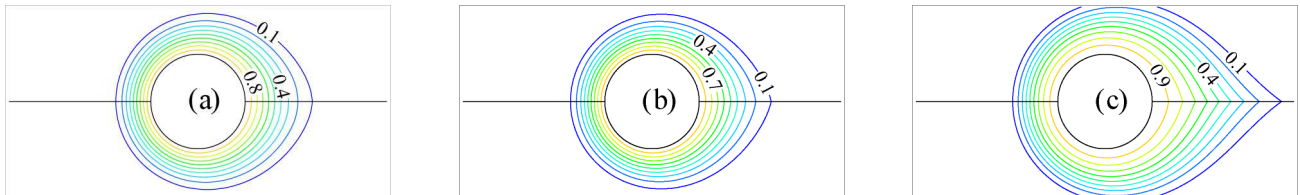


Fig. 7. Isotherms for $R_d=0.5$, $\Delta=0.5$, $M=0.1$, $\phi_1=0.1$, $\phi_2=0.05$ when (a) $Ri=0.0$, (b) $Ri=0.5$, and (c) $Ri=1.0$.

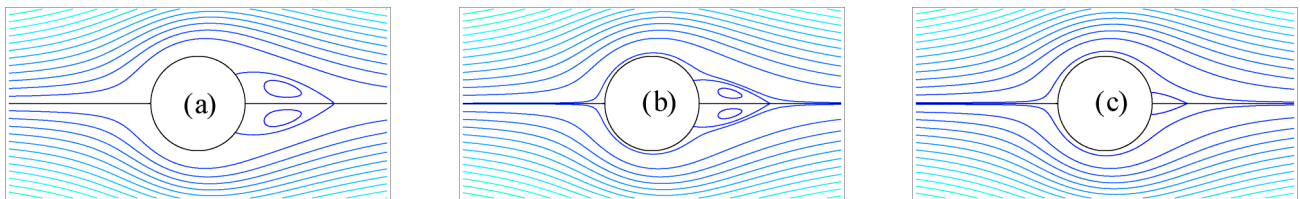


Fig. 8. Streamlines for $R_d=0.2$, $Ri=0.5$, $\Delta=0.2$, $\phi_1=0.1$, $\phi_2=0.05$ when (a) $M=0.0$, (b) $M=0.2$, (c) $M=0.5$.

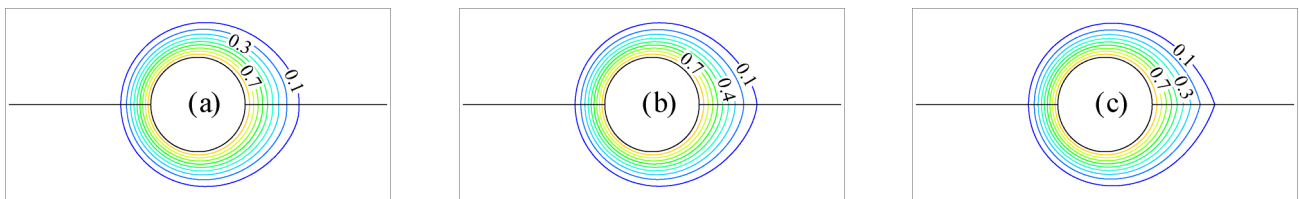


Fig. 9. Isotherms for $R_d=0.2$, $Ri=0.5$, $\Delta=0.2$, $\phi_1=0.1$, $\phi_2=0.05$ when (a) $M=0.0$, (b) $M=0.2$, (c) $M=0.5$.

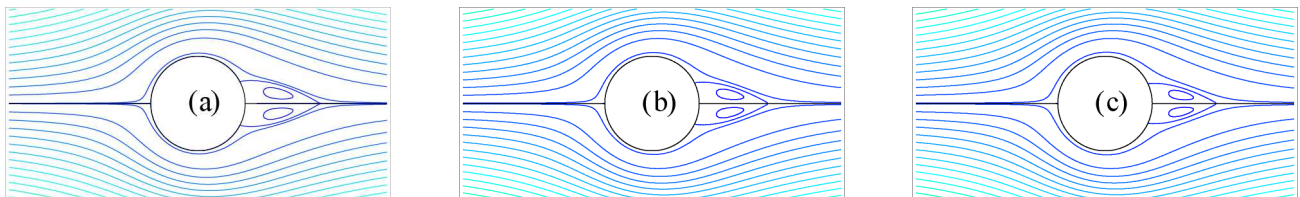


Fig. 10. Streamlines for $Ri=0.5$, $\Delta=0.2$, $M=0.1$, $\phi_1=0.1$, $\phi_2=0.05$ when (a) $R_d=0.0$, (b) $R_d=0.5$, (c) $R_d=2.0$.



Graphical representation of Figs. 8 and 9 exhibits the change in steady state isotherms and streamlines for different magnetic field parameters, M . Here it is recognized that an increase in M lessens the covering area of vortex. The reason behind this fact is the delay of boundary layer separation for higher values of M and it happens because of the reduction in flow velocity with the increase of magnetic strength. On the other side, Fig. 9 depicts that the impact of M on isotherms is not so irresistible; that is, isotherms are slightly condensing for increased values of M .

The R_d effects on steady state streamlines and isotherms are respectively illustrated in Figs. 10 and 11. Figures 10(a)-(c) clearly outline that increasing values of R_d reduce vortex size. Increasing the thermal radiation hinders the flow separation and due to the decrease of separation point the vortex size diminishes. However, isothermal lines from Figs. 11(a)-(c) are elongating rapidly for the amplifying heat transfer rate in hybrid nanofluid. Along free stream velocity, it is noticed that larger R_d values progressively assist the fluid flow to thicken the thermal boundary layer.

Figures 12 and 13 depict the influences of Δ on steady state streamlines and isotherms. Figure 12 brings out the fact that vortex area is reducing steadily for higher values of Δ . This is due to the late occurrence of boundary layer separation and therefore vortex area is diminishing. However, the system temperature is drastically changing around the cylinder due to accelerated Δ . We found from Fig. 13 that isothermal lines are rapidly widening for larger Δ values. It is noted here that higher values of Δ implies larger surface temperature and so the higher heated fluid adjacent to the cylinder passes it near its surface resulting the reduction in boundary layer separation.

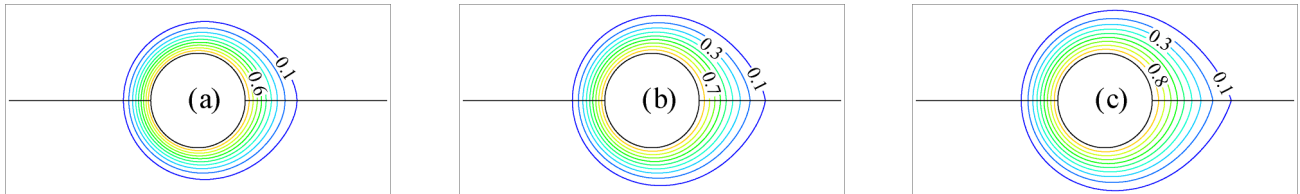


Fig. 11. Isotherms for $Ri=0.5$, $\Delta=0.2$, $M=0.1$, $\phi_1=0.1$, $\phi_2=0.05$ when (a) $R_d=0.0$, (b) $R_d=0.5$, (c) $R_d=2.0$.

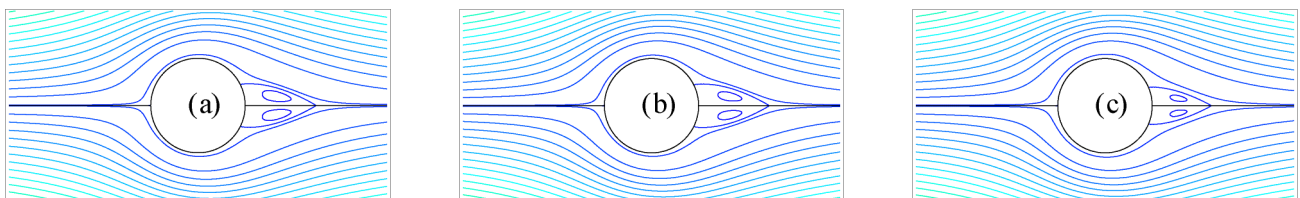


Fig. 12. Streamlines for $R_d=0.5$, $Ri=0.5$, $M=0.1$, $\phi_1=0.1$, $\phi_2=0.05$ when (a) $\Delta=0.0$, (b) $\Delta=0.5$, (c) $\Delta=1.0$.

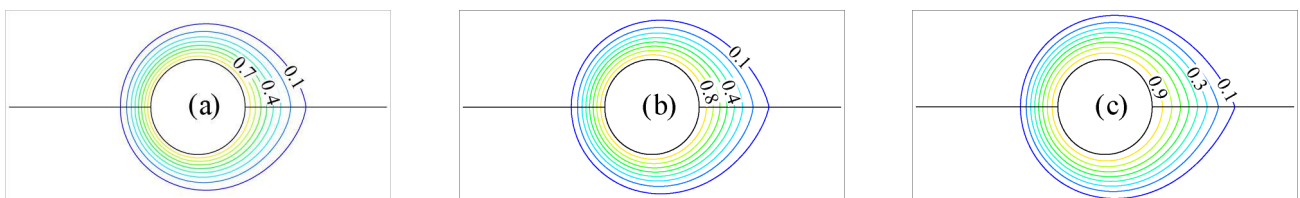


Fig. 13. Isotherms for $R_d=0.5$, $Ri=0.5$, $M=0.1$, $\phi_1=0.1$, $\phi_2=0.05$ when (a) $\Delta=0.0$, (b) $\Delta=0.5$, (c) $\Delta=1.0$.

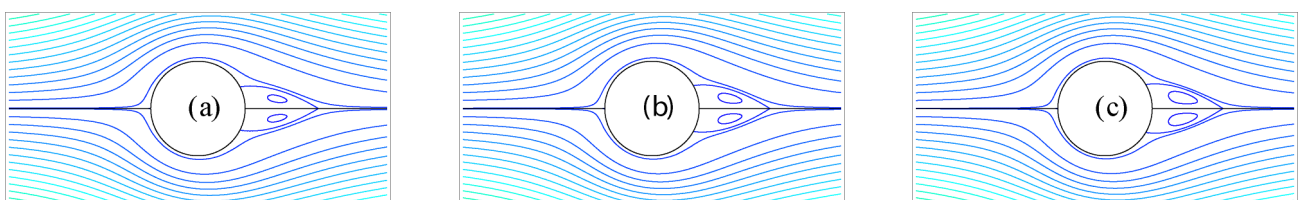


Fig. 14. Streamlines for $R_d=0.2$, $Ri=0.2$, $\Delta=0.2$, $M=0.1$, $\phi_1=0.1$ when (a) $\phi_2=0.0$, (b) $\phi_2=0.05$, (c) $\phi_2=0.1$.

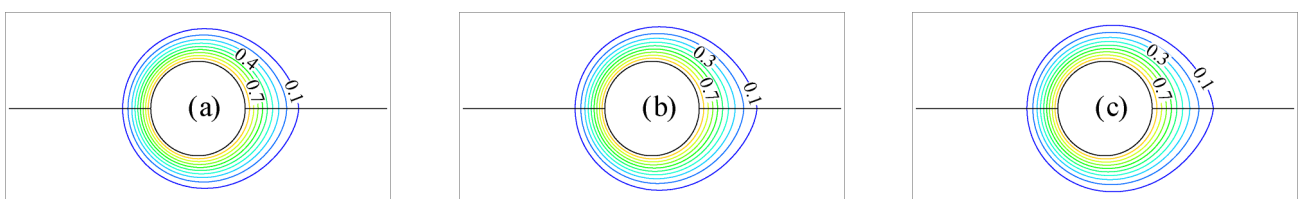


Fig. 15. Isotherms for $R_d=0.2$, $Ri=0.2$, $\Delta=0.2$, $M=0.1$, $\phi_1=0.1$ when (a) $\phi_2=0.0$, (b) $\phi_2=0.05$, (c) $\phi_2=0.1$.



The changes of steady state streamlines and isotherms due to the effect of varying ϕ_2 are depicted in Figs. 14-15. From the Figs. 14(a)-(c), it is perceived that larger ϕ_2 accelerates the separation of flow. Besides, its effect on isotherms indicates that heat is transferred to the downstream region for higher values of ϕ_2 and so it is inspected that substantial heat transfer occurs in hybrid nanofluid. The reasons for such characteristics are that when more nanoparticles are dispersed into the base fluid, the exerted force by the nanoparticles leads to quick separation of the flow from the surface of the cylinder.

Effects of ϕ_1 on steady state streamlines and isotherms are displayed in Figs. 16(a)-(c) and 17(a)-(c). Interpretation of Fig. 16 comes out with the fact that higher values of ϕ_1 diminish vortex region slightly. This scenario occurs due to the accelerated flow separation for increased ϕ_1 values. Hence it is recognized that comparatively larger vortex area is found in Fig. 16(a) because of the earlier flow separation. Moreover, isothermal lines are more elongating for enhanced values of ϕ_1 . This result elucidates that thermal boundary layer gets thicker for increasing ϕ_1 .

4.2 Variations of the skin friction coefficients and local Nusselt number with parameters

Figures 18(a) and 18(b) illustrate $(1/2)Re^{1/2}C_f$ and $Re^{-1/2}Nu$ against X for varying time ξ . Here we notice that both $(1/2)Re^{1/2}C_f$ and $Re^{-1/2}Nu$ decrease with the increase of time and after a certain time they reach the steady state. For $\xi > 0.5$, $(1/2)Re^{1/2}C_f$ decreases slowly and attains a negative value along the streamwise direction. This indicates that velocity gradient becomes zero near the rear front of the cylinder and reverse flow exists just behind the cylinder. We can also conclude from graphical representation that there is a peak value near $X = 85^\circ$, a minimum value near $X = 162^\circ$ and point of separations are happening for $\xi > 0.8$. The fact for this scenario is the precipitate eruption of hybrid nanofluid due to the presence of thermally driven cylinder in it.

The impacts of Ri on $(1/2)Re^{1/2}C_f$ and $Re^{-1/2}Nu$ against X are depicted in Figs. 19(a, b). These illustrations imply that for larger Ri , both $(1/2)Re^{1/2}C_f$ and $Re^{-1/2}Nu$ significantly increase. Taking $Ri = 0.0, 0.5$ and 1.0 , it is found that point of separation moves away from the front stagnation point ($X=0$) successively to assist the fluid flow. It happens due to the strong buoyancy force driven by higher Ri values. When hybrid nanofluid is used we find the maximum values of $(1/2)Re^{1/2}C_f$ and $Re^{-1/2}Nu$ for $Ri = 0.0$ and 0.5 as (1.1834, 2.9712) and (1.3148, 3.0340). Whereas using Al_2O_3 -water nanofluid relating to $\phi_1 = 0.1$ and $\phi_2 = 0.0$, we find that the corresponding values for $Ri = 0.0$ and 0.5 are (0.9658, 2.4411) and (1.1010, 2.5060). The increments in $(1/2)Re^{1/2}C_f$ for $Ri = 0.0, 0.5$ using hybrid nanofluid and nanofluid are about 13.14% and 13.52% whereas those in $Re^{-1/2}Nu$ are 6.28% and 6.5%. It implies the fact that Ri impact on $(1/2)Re^{1/2}C_f$ is more substantial than on $Re^{-1/2}Nu$ in both cases and no prominent effect is found in hybrid nanofluid in comparison to use nanofluid.

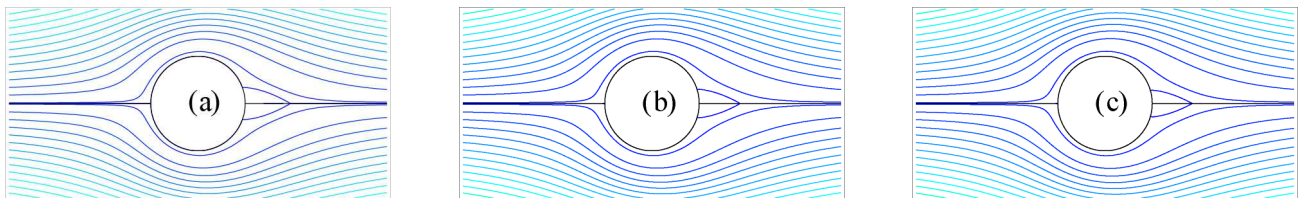


Fig. 16. Streamlines for $Ri=0.2$, $\Delta=0.2$, $M=0.2$, $\phi_2=0.1$ when (a) $\phi_1=0.0$, (b) $\phi_1=0.05$, (c) $\phi_1=0.1$.

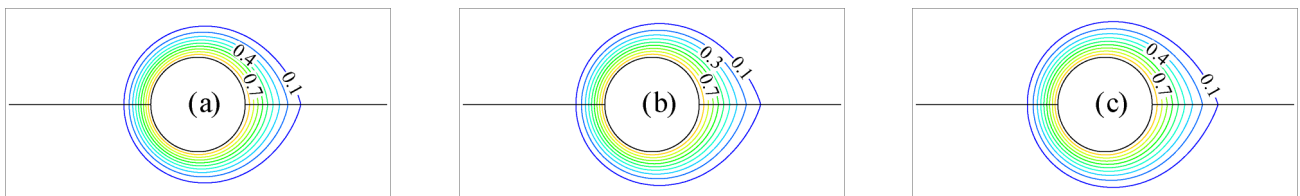


Fig. 17. Isotherms for $Ri=0.2$, $\Delta=0.2$, $M=0.2$, $\phi_2=0.1$ when (a) $\phi_1=0.0$, (b) $\phi_1=0.05$, (c) $\phi_1=0.1$.

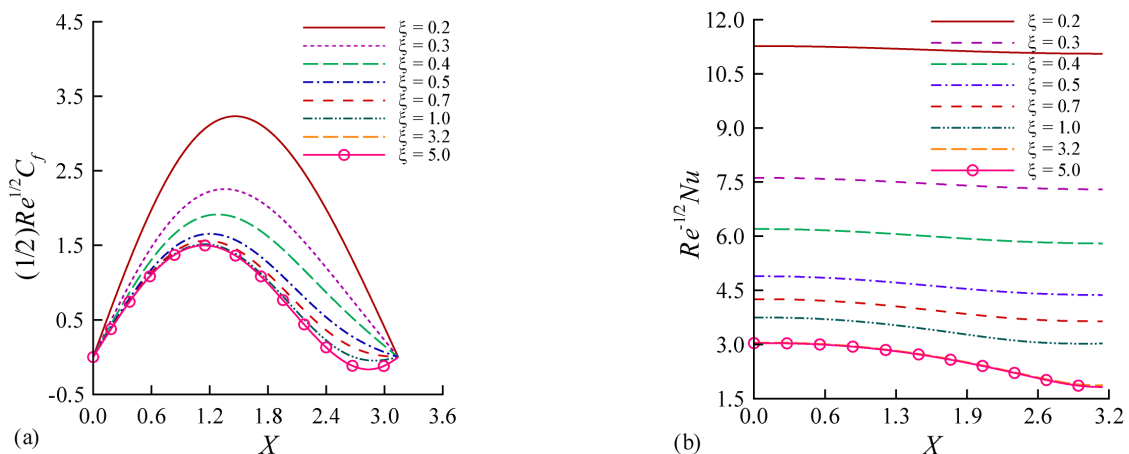


Fig. 18. (a) skin friction coefficient and (b) Nusselt number for different values of X for different time period ξ when $Ri=0.1$, $R_d=0.5$, $\Delta=0.5$, $M=0.1$, $\phi_1=0.1$, $\phi_2=0.05$.



In Figs. 20(a, b), the impacts of M on $(1/2)Re^{1/2}C_f$ and $Re^{-1/2}Nu$ are elucidated. These figures yield that $(1/2)Re^{1/2}C_f$ and $Re^{-1/2}Nu$ both are increasing due to increased M values. Along streamwise direction, flow separation point is seen extremely high for smaller M values. Since we consider hybrid nanofluid, the maximum $(1/2)Re^{1/2}C_f$ and $Re^{-1/2}Nu$ values without M are (1.1939, 1.8929) and the corresponding values for $M=0.5$ are (1.3668, 1.9418). Therefore the values of $(1/2)Re^{1/2}C_f$ and $Re^{-1/2}Nu$ are increased about 17.29% and 4.89%, respectively. On the contrary, the maximum values of $(1/2)Re^{1/2}C_f$ and $Re^{-1/2}Nu$ using Al_2O_3 -water nanofluid for $M=0.0$ and 0.5 are (0.9819, 1.6108) and (1.1303, 1.6564) and so the increments are about 14.84% and 4.56%. Accordingly, maximum increment in $(1/2)Re^{1/2}C_f$ for hybrid nanofluid is found larger than using nanofluid. Also, the results signify that magnetic field parameter M performs more effectively on $(1/2)Re^{1/2}C_f$ than on $Re^{-1/2}Nu$.

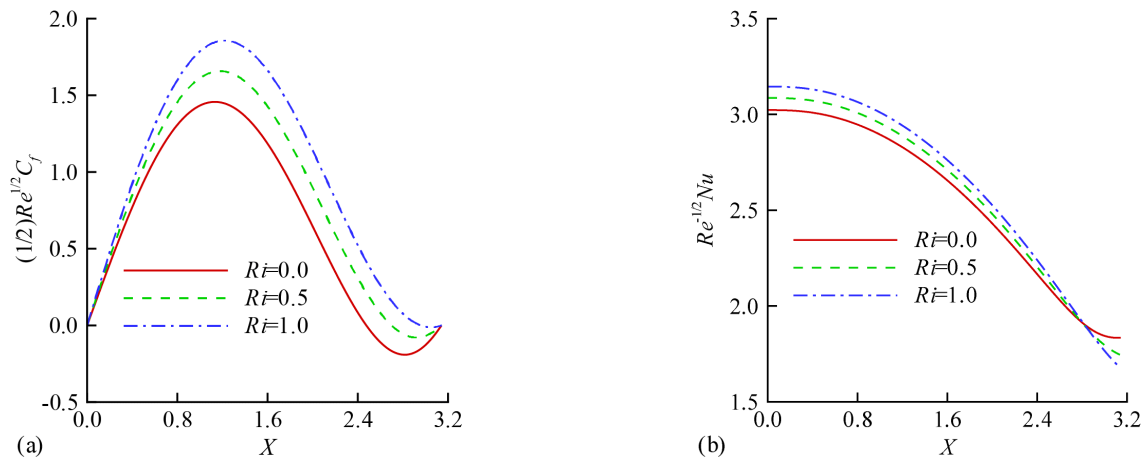


Fig. 19. Effect of Ri on (a) skin friction coefficient and (b) Nusselt number when $R_d=0.5$, $\Delta=0.5$, $M=0.1$, $\phi_1=0.1$, $\phi_2=0.05$.

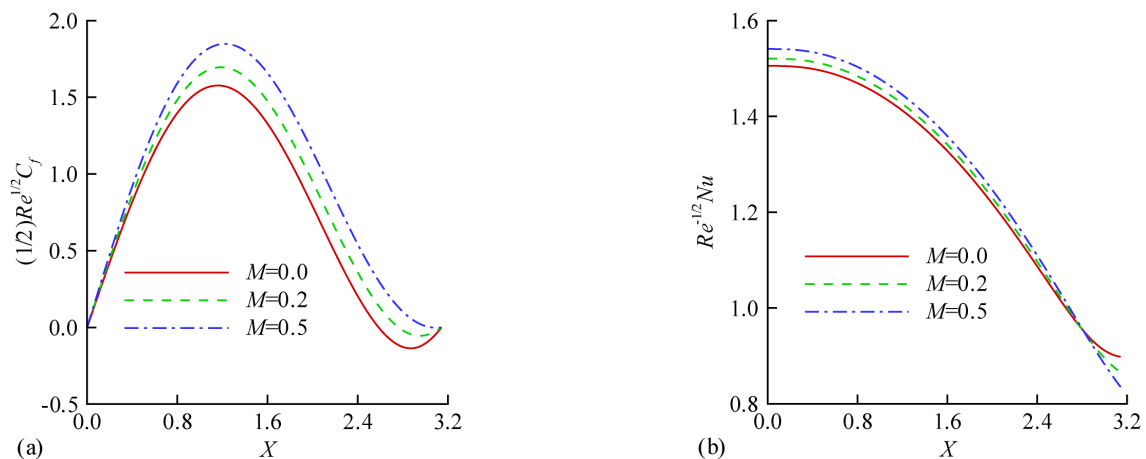


Fig. 20. Effect of M on (a) skin friction coefficient and (b) Nusselt number when $R_d=0.2$, $Ri=0.2$, $\Delta=0.2$, $\phi_1=0.1$, $\phi_2=0.05$.

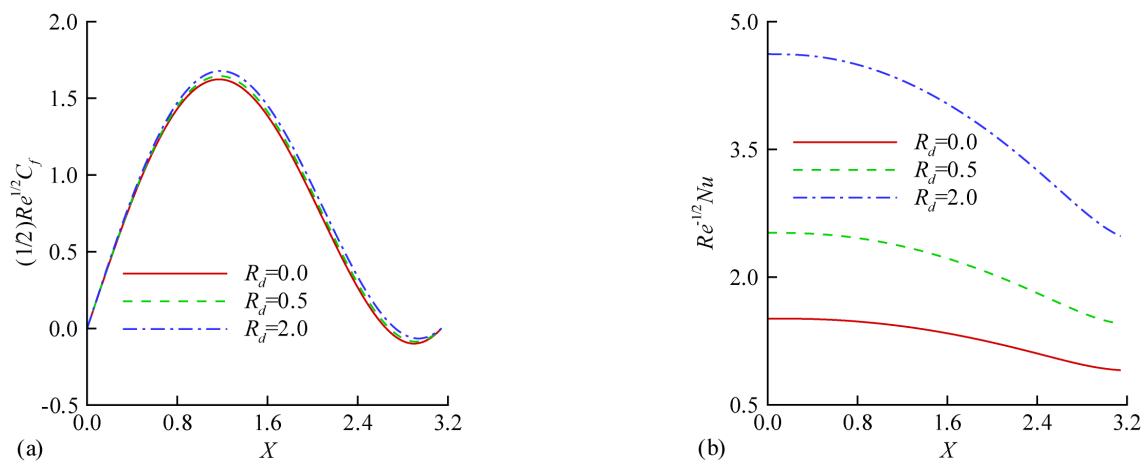


Fig. 21. Effect of R_d on (a) skin friction coefficient and (b) Nusselt number when $Ri=0.5$, $\Delta=0.2$, $M=0.1$, $\phi_1=0.1$, $\phi_2=0.05$.



To understand the R_d mechanism on $(1/2)Re^{1/2}C_f$ and $Re^{-1/2}Nu$, a bunch of R_d values have been taken in Figs. 21(a, b). Here R_d acts in accordance with the aforesaid quantities $Ri=0.5$, $\Delta=0.2$, $M=0.1$ and $\phi_1=0.1$, $\phi_2=0.05$. These illustrations emphasize that for ascending R_d values, separation point leads towards the rear stagnation point. It happens due to dynamic radiative heat emission driven by hybrid nanofluid particles from the heated surface to the adjoining area. The impact on $Re^{-1/2}Nu$ is found as very strong nature for increased R_d values. As we use (Cu-Al₂O₃/water) hybrid nanofluid, the maximum $(1/2)Re^{1/2}C_f$ and $Re^{-1/2}Nu$ values for $R_d=0.0$ and 0.5 are (1.2934, 1.4904) and (1.3069, 2.4792). Here the increased quantities are 1.35% and 98.88%. Contrary to this, using Al₂O₃-water nanofluid, $(1/2)Re^{1/2}C_f$ and $Re^{-1/2}Nu$ values for $R_d=0.0, 0.5$ are (1.0753, 1.3001) and (1.0919, 2.0834). The corresponding increments are 1.69% and 78.33%. Therefore, by taking larger R_d values, increment in $(1/2)Re^{1/2}C_f$ for hybrid nanofluid is obtained lower than using Al₂O₃-water nanofluid but the increment in $Re^{-1/2}Nu$ for hybrid nanofluid is higher than for Al₂O₃-water nanofluid.

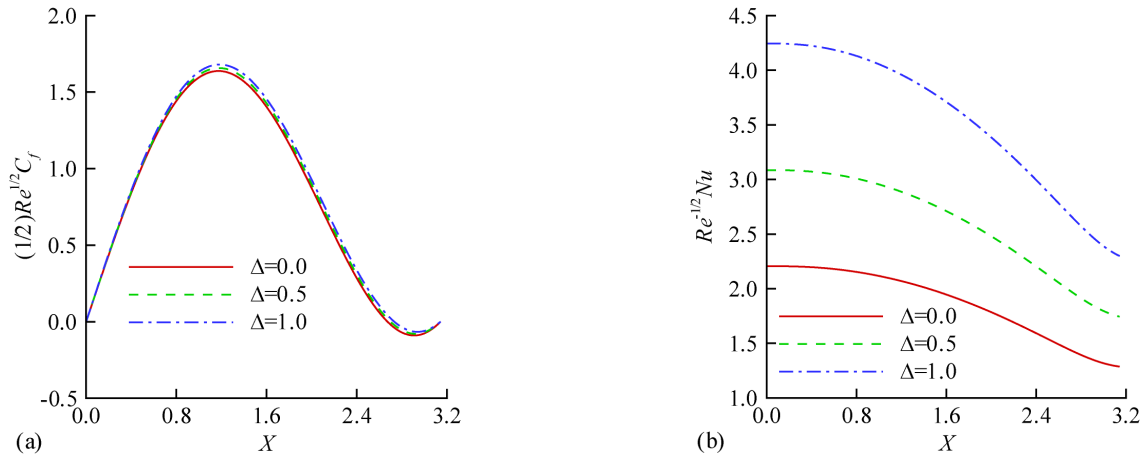


Fig. 22. Effect of Δ on (a) skin friction coefficient and (b) Nusselt number when $R_d=0.5$, $Ri=0.5$, $M=0.1$, $\phi_1=0.1$, $\phi_2=0.05$.

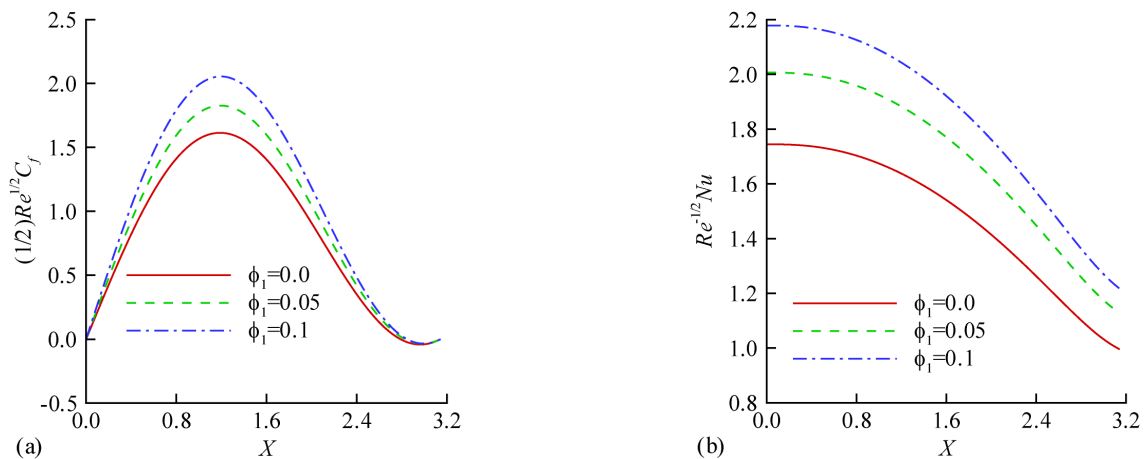


Fig. 23. Effect of ϕ_1 on (a) skin friction coefficient and (b) Nusselt number when $R_d=0.2$, $Ri=0.2$, $\Delta=0.2$, $M=0.2$, $\phi_2=0.1$.

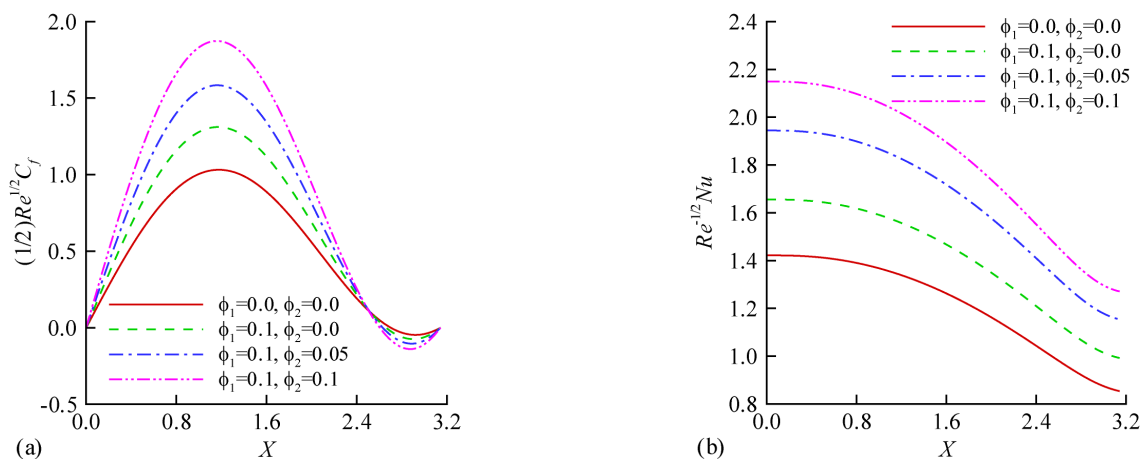


Fig. 24. Effect of ϕ_2 on (a) skin friction coefficient and (b) Nusselt number when $R_d=0.2$, $Ri=0.2$, $\Delta=0.2$, $M=0.1$, $\phi_1=0.1$.



Table 2. Separation points for different values of the parameters

ϕ_1	ϕ_2	Ri	M	R_d	Δ	Point of Separation (S_p)
0.0	0.1	0.2	0.2	0.2	0.2	165.7°
0.02						166.7°
0.04						166.7°
0.06						166.7°
	0.0					171.0°
	0.02					170.3°
	0.04					169.3°
	0.06					168.3°
	0.08					167.3°
	0.05	0.0				162.7°
		0.1				165.7°
		0.3				172.0°
		0.4				175.3°
		0.5				179.0°
		0.2	0.0			145.3°
			0.2			150.0°
			0.4			163.3°
			0.6			178.3°
			0.2	0.0		168.0°
				0.5		169.3°
				1.0		170.3°
				2.0		171.0°
				5.0		172.7°
				0.2	0.0	168.7°
					0.5	169.0°
					1.0	169.3°
					2.0	170.3°

Figures 22(a, b) stand for identifying Δ impacts on $(1/2)Re^{1/2}C_f$ and $Re^{-1/2}Nu$. Fig 22(a) declares that by increasing surface temperature parameter, Δ , the point of separation becomes weak in nature. Attaining a minimum negative value at every single level, each separation point occurs near $X=168^\circ$. It is also perceived that Δ effect on $(1/2)Re^{1/2}C_f$ is not so strong in nature. On the other hand, $Re^{-1/2}Nu$ values increase rapidly owing to the increment of Δ in energy equation. For hybrid nanofluid, the maximum $(1/2)Re^{1/2}C_f$ and $Re^{-1/2}Nu$ values for $\Delta=0.0, 0.5$ are (1.3024, 2.1715) and (1.3148, 3.0340). The augmentation in $(1/2)Re^{1/2}C_f$ is then obtained as 1.24% and the increase in $Re^{-1/2}Nu$ is 86.25%. Moreover, considering Al_2O_3 -water nanofluid, corresponding values are (1.0865, 1.8525) and (1.1010, 2.5061). Hence the increase in $(1/2)Re^{1/2}C_f$ is 1.45% and for $Re^{-1/2}Nu$ is 65.36%. Therefore the result leads to the decision that influence of surface temperature parameter on $Re^{-1/2}Nu$ in hybrid nanofluid is so noteworthy than using nanofluid while on $(1/2)Re^{1/2}C_f$, opposite characteristic is found.

Figures 23(a, b) illustrate ϕ_1 effects on $(1/2)Re^{1/2}C_f$ and $Re^{-1/2}Nu$. These figures indicate that increased ϕ_1 values enhance both $(1/2)Re^{1/2}C_f$ and $Re^{-1/2}Nu$ values. From skin friction factor profile, it is pointed that separation points are changed a little bit for increasing volume fraction of nanoparticle ϕ_1 and each of them occurs near $X=165^\circ$. However, the impact of ϕ_1 on $Re^{-1/2}Nu$ is strong and it causes a substantial increase in $Re^{-1/2}Nu$. As hybrid nanofluid is taken, the maximum values of $(1/2)Re^{1/2}C_f$ and $Re^{-1/2}Nu$ for $\phi_1=0.1$ are (1.5015, 2.1148). For Cu-water nanofluid, corresponding values are (1.1980, 1.6972). In addition, when water is used maximum values of $(1/2)Re^{1/2}C_f$ and $Re^{-1/2}Nu$ are (0.8177, 1.4007). Hence, the decision terminates in the fact that values of $Re^{-1/2}Nu$ are 41.76% larger in hybrid nanofluid rather than utilizing Cu-water nanofluid and 71.41% higher than the base fluid.

In order to apprehend the influence of ϕ_2 on $(1/2)Re^{1/2}C_f$ and $Re^{-1/2}Nu$, Figs. 24(a, b) have been drawn. With the increase of the volume fraction of nanoparticle ϕ_2 , it is identified that values of $(1/2)Re^{1/2}C_f$ increase significantly. In addition, we find that flow separation occurs quickly for larger ϕ_2 . Moving towards to the rear stagnation point, every separation point is occurred near $X=163^\circ$ and the peak value of $(1/2)Re^{1/2}C_f$ is found near $X=68^\circ$. Furthermore, the varying ϕ_2 affects $Re^{-1/2}Nu$ strongly. As we see from Fig. 24(b) that $Re^{-1/2}Nu$ increases successively for increased ϕ_2 values. When hybrid nanofluid is used, the maximum values of $(1/2)Re^{1/2}C_f$ and $Re^{-1/2}Nu$ for $\phi_1=0.1$ and $\phi_2=0.05$ are (1.2303, 1.9036) and using Al_2O_3 -water nanofluid, corresponding values of $(1/2)Re^{1/2}C_f$ and $Re^{-1/2}Nu$ become (1.0132, 1.6208). When pure fluid is considered, then maximum values of $(1/2)Re^{1/2}C_f$ and $Re^{-1/2}Nu$ are (0.7935, 1.3921). These results suggest that hybrid nanofluid yields 28.28% higher heat transfer than using Al_2O_3 -water nanofluid and 51.15% higher than pure fluid.

4.3 Effects of parameters on boundary layer separation

In Table 2, the variations of the point of separation of the boundary layer from the cylinder surface are presented with the change of the pertinent parameters. It is evident from the table that the boundary layer separation is accelerated with the increase of ϕ_2 , however it remains constant for $\phi_1>0.02$. The cause is that the inclusion of alumina nanoparticles into the base fluid changes the thermophysical properties of the hybrid nanofluid which leads to separate the boundary from the cylinder wall. However, increasing in Ri, M, R_d and Δ causes a delay in the separation of the boundary layer from the cylinder surface.

5. Conclusions

Unsteady magnetohydrodynamic mixed convection flow across a cylinder has been studied for Cu- Al_2O_3 /water hybrid nanofluid. Utilizing finite difference scheme, the dimensionless governing equations are solved. In addition, asymptotic and perturbation procedures are performed respectively for long time and short time and the comparison shows an excellent agreement with the numerical solution. According to the results, the conclusions are summarized below:

- With the increase of Ri, values of $(1/2)Re^{1/2}C_f$ and $Re^{-1/2}Nu$ are found to increase and the boundary layer separation becomes delay by moving the point of separation further to the rear stagnation point and the vortex size diminishes.
- Values of $(1/2)Re^{1/2}C_f$ and $Re^{-1/2}Nu$ are significantly increased for higher values of M. Also, an increase in M reduces the vortex



- size and delays the boundary layer separation but causes an elongation of isothermal lines.
- iii. Due to amplified R_d , vorticities are monotonically decreasing due to the delay of flow separation, while more temperature go downstream.
 - iv. Higher Δ enhances the values of $(1/2)Re^{1/2}C_f$ and $Re^{-1/2}Nu$. Moreover, the occurrence of boundary layer separation becomes delay with the increase of Δ .
 - v. Owing to the larger values of ϕ_1 and ϕ_2 , the heat transfer is significantly increased in comparison to the nanofluid and the carrier fluid. Contrary to this, the addition of alumina nanoparticles into the base fluid augments the boundary layer separation.

Author Contributions

Nepal Chandra Roy developed the mathematical modeling, scheme, code of the problem and examined theory validation; Aysha Akter derived equations of mathematical modeling and examined the theory validation. The manuscript was written through the contribution of all authors. All authors discussed the results, reviewed, and approved the final version of the manuscript.

Acknowledgments

Aysha Akter would like to express her sincere appreciation to the Ministry of Science and Technology (MOST), Government of the People's Republic of Bangladesh for providing her the NST fellowship for conducting this research.

Conflict of Interest

The authors declared no potential conflicts of interest with respect to the research, authorship, and publication of this article.

Funding

The authors received no financial support for the research, authorship, and publication of this article.

Data Availability Statements

The datasets generated and/or analyzed during the current study are available from the corresponding author on reasonable request.

References


- [1] Udhayakumar, S., Rejeesh, A., D., A., Sekhar, T., V., S., Sivakumar, R., Numerical investigation of magnetohydrodynamic mixed convection over an isothermal circular cylinder in presence of an aligned magnetic field, *International Journal of Heat and Mass Transfer*, 95, 2016, 379–392.
- [2] Abel, M., S., Tawade, J., V., Shinde, J., N., The effects of MHD flow and heat transfer for the UCM fluid over a stretching surface in presence of thermal radiation, *Advances in Mathematical Physics*, 702681, 2012, 1–21.
- [3] Aldoss, T. K., Ali, Y. D., Al-Nimr, M. A., MHD mixed convection from a horizontal circular cylinder, *Numerical Heat Transfer, Part A: Applications*, 30(4), 1996, 379–396.
- [4] Hasan, N., Ali, R., Steady and unsteady flow regimes in two-dimensional mixed convective flow of air past a heated square cylinder, *International Journal of Mechanical Sciences*, 175, 2020, 105533.
- [5] Roy, N., C., Rahman, T., Parvin, S., Boundary-Layer separations of mixed convection flow past an isothermal circular cylinder, *International Journal of Applied and Computational Mathematics*, 5(3), 2019, 48.
- [6] Azim, N., A., Chowdhury, M., K., MHD-conjugate free convection from an isothermal horizontal circular cylinder with Joule heating and heat generation, *Journal of Computational Methods in Physics*, 180516, 2013, 1–11.
- [7] Sharma, N., Dhiman, A. K., Kumar, S., Mixed convection flow and heat transfer across a square cylinder under the influence of aiding buoyancy at low Reynolds numbers, *International Journal of Heat and Mass Transfer*, 55, 2012, 2601–2614.
- [8] Das, S., Tarafdar, B., Jana, R., N., Makinde, O.D., Influence of rotational buoyancy on magneto-radiation-convection near a rotating vertical plate, *European Journal of Mechanics / B Fluids*, 75, 2019, 209–218.
- [9] Chaabane, R., Askri, F., Nasrallah, S., B., Application of the lattice Boltzmann method to transient conduction and radiation heat transfer in cylindrical media, *Journal of Quantitative Spectroscopy and Radiative Transfer*, 112, 2011, 2013–2027.
- [10] Wang, T., Y., Kleinstreuer, C., Local skin friction and transfer in combined free-forced convection from a cylinder or sphere to a power-law fluid, *International Journal of Heat and Fluid Flow*, 9(2), 1988, 182–187.
- [11] Mucoglu, A., Chen, T., S., Analysis of combined forced and free convection across a horizontal cylinder, *The Canadian Journal of Chemical Engineering*, 55(3), 1977, 265–271.
- [12] Choi, S., U., Eastman, J., Enhancing thermal conductivity of fluids with nanoparticles, *ASME International Mechanical Engineering Congress and Exposition*, 231, 1995, 99–105.
- [13] Sachica, D., Trevino, C., Suastegui, L., M., Numerical study of magnetohydrodynamic mixed convection and entropy generation of Al_2O_3 -water nanofluid in a channel with two facing cavities with discrete heating, *International Journal of Heat and Fluid Flow*, 86, 2020, 108713.
- [14] Hosseinzadeh, K., Asadi, A., Mogharrebi, A., R., Khalesi, J., Mousavisani, S., Ganji, D., D., Entropy generation analysis of $(CH_3OH)_2$ containing CNTs nanofluid flow under effect of MHD and thermal radiation, *Case Studies in Thermal Engineering*, 14, 2019, 100482.
- [15] Mkhathshwa, M., P., Motsa, S., S., Ayano, M., S., Sibanda, P., MHD mixed convective nanofluid flow about a vertical slender cylinder using overlapping multi-domain spectral collocation approach, *Case Studies in Thermal Engineering*, 18, 2020, 100598.
- [16] Hayat, T., Ullaha, H., Ahmadb, B., Alhodalyb, M., S., Heat transfer analysis in convective flow of Jeffrey nanofluid by vertical stretchable cylinder, *International Communications in Heat and Mass Transfer*, 120, 2021, 104965.
- [17] Nagendramma, V., Leelarathnam, A., Raju, C., S., K., Shehzad, S., A., Hussain, T., Doubly stratified MHD tangent hyperbolic nanofluid flow due to permeable stretched cylinder, *Results in Physics*, 9, 2018, 23–32.
- [18] Roy, N., C., Magnetohydrodynamic natural convection flow of a nanofluid due to sinusoidal surface temperature variations, *Physics of Fluids*, 32, 2020, 022003.
- [19] Sheikholeslami, M., Jafaryar, M., Said, Z., Alsabery, A., I., Babazadeh, H., Shafee, A., Modification for helical turbulator to augment heat transfer behavior of nanomaterial via numerical approach, *Applied Thermal Engineering*, 182, 2021, 115935.
- [20] M. Sheikholeslami, M., Farshad, S., A., Said, Z., Analyzing entropy and thermal behavior of nanomaterial through solar collector involving new tapes, *International Communications in Heat and Mass Transfer*, 123, 2021, 105190.
- [21] M. Sheikholeslami, M., Farshad, S., A., Ebrahimpour, Z., Said, Z., Recent progress on flat plate solar collectors and photovoltaic systems in the presence of nanofluid: A review, *Journal of Cleaner Production*, 293, 2021, 126119.
- [22] Jamil, F., Ali, H., M., Applications of hybrid nanofluids in different fields, *Hybrid Nanofluids for Convection Heat Transfer*, 2020, 215–254.
- [23] Jana, S., Khojin, A., S., Zhong, W., H., Enhancement of fluid thermal conductivity by the addition of single and hybrid nano-additives, *Thermochimica Acta*, 462(1–2), 2007, 45–55.



- [24] Zainal, N., A., Nazara, R., Naganthana, K., Pop, I., MHD mixed convection stagnation point flow of a hybrid nanofluid past a vertical flat plate with convective boundary condition, *Chinese Journal of Physics*, 66, 2020, 630–644.
- [25] Alharbi, S. O., Nawaz, M., Nazir, U., Thermal analysis for hybrid nanofluid past a cylinder exposed to magnetic field, *AIP Advances*, 9, 2019, 115022.
- [26] Khashi'ie, N., S., Arifin, N., M., Pop, I., Wahid, N., S., Flow and heat transfer of hybrid nanofluid over a permeable shrinking cylinder with Joule heating: A comparative analysis, *Alexandria Engineering Journal*, 59, 2020, 1787–1798.
- [27] Abbas, N., Nadeem, S., Saleem, A., Malik, M., Y., Issakhov, A., Alharbi, F., M., Models base study of inclined MHD of hybrid nanofluid flow over nonlinear stretching cylinder, *Chinese Journal of Physics*, 69, 2021, 109–117.
- [28] Devi, S., S., U., Devi, S., P., A., Numerical investigation of three-dimensional hybrid Cu-Al₂O₃/ water nanofluid flow over a stretching sheet with effecting Lorentz force subject to Newtonian heating, *Canadian Journal of Physics*, 94(5), 2016, 490–496.
- [29] Shoaib, M., Raja, M., A., Z., Sabir, M., T., Awais, M., Islam, S., Shah, Z., Kumam, P., Numerical analysis of 3-D MHD hybrid nanofluid over a rotational disk in presence of thermal radiation with Joule heating and viscous dissipation effects using Lobatto IIIA technique, *Alexandria Engineering Journal*, 60, 2021, 3605–3619.
- [30] Rashid, U., Liang, H., Ahmad, H., Abbas, M., Iqbal, A., Hamed, Y., S., Study of (Ag and TiO₂)/water nanoparticles shape effect on heat transfer and hybrid nanofluid flow toward stretching shrinking horizontal cylinder, *Results in Physics*, 21, 2021, 103812.
- [31] Ghalambaz, M., Groşan, T., Pop, I., Mixed convection boundary layer flow and heat transfer over a vertical plate embedded in a porous medium filled with a suspension of nano-encapsulated phase change materials, *Journal of Molecular Liquids*, 293, 2019, 111432.
- [32] Ghalambaz, M., Mehryan, S., A., M., Hajjar, A., Veisimoradi, A., Unsteady natural convection flow of a suspension comprising Nano-Encapsulated Phase Change Materials (NEPCMs) in a porous medium, *Advanced Powder Technology*, 31(3), 2020, 954–966.
- [33] Mehryana, S., A., M., Ghalambaz, M., Gargari, L., S., Hajjar, A., Sheremet, M., Natural convection flow of a suspension containing nano-encapsulated phase change particles in an eccentric annulus, *Journal of Energy Storage*, 28, 2020, 101236.
- [34] Hajjar, A., Mehryan, S., A., M., Ghalambaz, M., Time periodic natural convection heat transfer in a nano-encapsulated phase-change suspension, *International Journal of Mechanical Sciences*, 166, 2020, 105243.
- [35] Ghalambaz, M., Sheremet, M., A., Mehryan, S., A., M., Kashkooli, F., M., Pop I., Local thermal non-equilibrium analysis of conjugate free convection within a porous enclosure occupied with Ag-MgO hybrid nanofluid, *Journal of Thermal Analysis and Calorimetry*, 135, 2019, 1381–1398.
- [36] Mehryan, S., A., M., Ghalambaz, M., Chamkha, A., J., Izadi, M., Numerical study on natural convection of Ag-MgO hybrid/water nanofluid inside a porous enclosure: A local thermal non-equilibrium model, *Powder Technology*, 367, 2020, 443–455.
- [37] Brown, S., N., The effect of heat transfer on boundary-layer growth, *Mathematical Proceedings of the Cambridge Philosophical Society*, 59(4), 1963, 789–802.
- [38] Nazar, R., Amin, N., Pop, I., Mixed convection boundary-layer flow from a horizontal circular cylinder with a constant surface heat flux, *Heat and Mass Transfer*, 40, 2004, 219–227.
- [39] Raptis, A., Flow of a micropolar fluid past a continuously moving plate by the presence of radiation, *International Journal of Heat and Mass Transfer*, 41(18), 1998, 2865–2866.
- [40] Awang, M. A. O., Riley, N., Unsteady free convection from a heated sphere at high Grashof number, *Journal of Engineering Mathematics*, 17(4), 1983, 355–365.
- [41] Roy, N. C., Hossain, M. A., Gorla, R. S. R., Unsteady free convection from a heated sphere in the presence of internal heat generation or absorption, *International Journal of Thermal Sciences*, 98, 2015, 237–244.
- [42] Blottner, F., G., Finite difference methods of solution of the boundary-layer equations, *AIAA Journal*, 8(2), 1970, 193–205.
- [43] Butcher, J. C., Implicit Runge-Kutta processes, *Mathematics of Computation*, 18, 1964, 50–55.
- [44] Naschtsheim, P. R., Swigert, P. Satisfaction of asymptotic boundary conditions in numerical solution of systems of non-linear equation of boundary layer type, NASA TN D-3004, 1965.
- [45] Sparrow, E. M., Yu, H. S., Local non-similarity thermal boundary layer solutions, *Journal of Heat Transfer*, 93(4), 1971, 328–334.
- [46] Schlichting, H., Gersten, K., Boundary-layer theory, Springer-Verlag, Berlin, 2017.

ORCID iD

Nepal Chandra Roy  <https://orcid.org/000-0002-5623-9614>

Aysha Akter  <https://orcid.org/0000-0002-5853-3593>



© 2021 Shahid Chamran University of Ahvaz, Ahvaz, Iran. This article is an open access article distributed under the terms and conditions of the Creative Commons Attribution-NonCommercial 4.0 International (CC BY-NC 4.0 license) (<http://creativecommons.org/licenses/by-nc/4.0/>).

How to cite this article: Roy N.C., Akter A. Heat Transfer Enhancement and Boundary Layer Separations for a Hybrid Nanofluid Flow past an Isothermal Cylinder, *J. Appl. Comput. Mech.*, 7(4), 2021, 2096–2112. <https://doi.org/10.22055/JACM.2021.37795.3087>

Publisher's Note Shahid Chamran University of Ahvaz remains neutral with regard to jurisdictional claims in published maps and institutional affiliations.

